

Mapping the coupling between tract reachability and cortical geometry of the human brain

Received: 22 April 2025

Accepted: 30 July 2025

Published online: 12 August 2025

 Check for updates

Deying Li^{1,2,3}, Andrew Zalesky^{4,5}, Yufan Wang^{1,2,3}, Haiyan Wang^{1,2}, Liang Ma^{1,2}, Luqi Cheng⁶, Tobias Banaschewski⁷, Gareth J. Barker⁸, Arun L. W. Bokde⁹, Rüdiger Brühl¹⁰, Sylvane Desrivieres¹¹, Herta Flor^{12,13}, Hugh Garavan¹⁴, Penny Gowland¹⁵, Antoine Grigis¹⁶, Andreas Heinz¹⁷, Hervé Lemaître^{16,18}, Jean-Luc Martinot¹⁹, Marie-Laure Paillère Martinot^{19,20}, Eric Artiges^{19,21}, Frauke Nees^{7,22}, Dimitri Papadopoulos Orfanos¹³, Luise Poustka²³, Michael N. Smolka^{13,24}, Nilakshi Vaidya^{13,25}, Henrik Walter¹⁷, Robert Whelan²⁶, Gunter Schumann^{24,27}, Tianye Jia^{27,28,29,30}, Congying Chu^{1,2} ✉, Lingzhong Fan^{1,2,3,31,32} ✉ & IMAGEN Consortium*

The study of cortical geometry and connectivity is prevalent in human brain research. However, these two aspects of brain structure are usually examined separately, leaving the essential connections between the brain's folding patterns and white matter connectivity unexplored. In this study, we aim to elucidate the fundamental links between cortical geometry and white matter tract connectivity. We develop the concept of tract-geometry coupling (TGC) by optimizing the alignment between tract connectivity to the cortex and multiscale cortical geometry. We confirm in two independent datasets that cortical geometry reliably characterizes tract reachability, and that TGC demonstrates high test-retest reliability and individual-specificity. Interestingly, low-frequency TGC is more heritable and behaviorally informative. Finally, we find that TGC can reproduce task-evoked cortical activation patterns and exhibits non-uniform maturation during youth. Collectively, our study provides an approach to mapping cortical geometry-connectivity coupling, highlighting how these two aspects jointly shape the connected brain.

White matter tracts in the human brain form anatomical connections between different regions, collectively constituting the human connectome^{1,2}. These tracts contribute to information integration and activity coordination across the cerebral cortex, facilitating complex cognitive functions^{3,4}. However, few studies have sought to elucidate the patterns by which white matter tracts connect different parts of the cerebral cortex, i.e., the tract reachability^{2,5,6}, represented by the probability of a tract terminating on the cortical surface. While the macroscale human connectome provides a detailed map of region-to-region connectivity, it

does not fully account for the spatial and morphological characteristics of the regions innervated by each tract^{7,8}. Furthermore, as posited by the tension-based theory, mechanical tension generated by axons interacts with cortical geometric patterning during morphogenesis^{9,10}, implying that white matter tracts may influence cortical geometry throughout development. Thus, establishing a link between these two aspects is critical to understanding evolving brain patterns across the lifespan.

Cortical gyrification begins during embryonic development and yields complex cortical geometry to maintain a large surface area

A full list of affiliations appears at the end of the paper. *A list of authors and their affiliations appears at the end of the paper.

✉ e-mail: congying.chu@ia.ac.cn; lingzhong.fan@ia.ac.cn

relative to the limited cranial volume^{11,12}, accompanied by substantial changes in white matter¹³. Evidence suggests that developmental increases in cortical gyrification are associated with disproportionate cortical expansion relative to subcortical structures¹⁴. White matter undergoes significant concurrent changes, including subplate thickening¹⁵, increasing complexity of cortico-cortical fibers, and the emergence of short association fibers around the gyri¹³. Recent studies have demonstrated that cortical geometry is linked to brain functions and behaviors^{16,17}, and its abnormal changes may be partly explained by axonal fibers^{18,19}. These findings underscore the coupling between cortical geometry and white matter tracts, implying a dynamic interplay that is crucial for normal brain development and function. However, the precise nature by which cortical geometry and connectivity are coupled remains unknown, let alone how this coupling develops over time. Thus, measures are needed to quantify the extent of this coupling.

Therefore, we here aimed to quantify the coupling between white matter tracts and cortical geometry in the human brain using high-quality multimodal MRI data. To characterize white matter tracts, we used diffusion-weighted MRI to derive the cortical projection patterns of each tract, referred to as tract reachability maps, that represent the spatial distribution of tract endpoints on the cortical surface. For cortical geometry, we adopted an approach consistent with recent studies^{20,21}, decomposing the cortical surface into a set of geometric eigenmodes. To quantify the coupling between tract reachability and cortical geometry, we implemented a linear model in which the geometric eigenmodes were used to reconstruct each tract's reachability map. The resulting set of reconstruction coefficients was defined as the tract-geometry coupling (TGC), providing a quantitative measure of the relationship between white matter pathways and cortical geometry. The logic of the subsequent analyses to validate and explore the biological significance of TGC is illustrated in Fig. 1.

In summary, we demonstrated that TGC exhibited high test-retest reliability and strong individual specificity. We further differentiated the contributions of high- and low-frequency eigenmodes to TGC across tract types and heritability strength. Importantly, TGC was shown to predict a range of individual behavioral measures, underscoring its biological relevance. Moreover, TGC was able to effectively reproduce task-evoked cortical activation patterns, highlighting its functional implications. Finally, we observed significant age-related changes in TGC, reflecting developmental effects on the coupling between cortical geometry and white matter tracts from childhood through adolescence. Taken together, our study not only provides an approach to quantify the coupling relationship between cortical geometry and white matter tracts but also underscores how these two interconnected aspects jointly shape the brain activation and individual behavior.

Results

Linking cortical geometry and tract reachability

We here provided an overview of the construction of TGC. A population-averaged template of the cortical surface was used to obtain cortical eigenmodes²¹ (Fig. S1), which were then employed to reconstruct the tract reachability map for each white matter tract. To generate the tract reachability map, we first used a pre-trained deep-learning model, TractSeg²², to delineate each white matter tract. The reachability of these tracts to the cortical surface was then quantified using the connectivity blueprint approach, in which tract volume was multiplied with a gray matter surface-to-whole brain tractogram²³. The rows of resulting matrix corresponded to the cortical projection patterns of white matter tracts, which is explicitly referred to as the “tract reachability map” in the following text. Note that the superior cerebellar peduncle (SCP), middle cerebellar peduncle (MCP), inferior cerebellar peduncle (ICP), and fornix (FX) were disregarded because of

their absence of projection to the cortex, and overall corpus callosum (CC—all) was excluded as its seven subsections were already available. Therefore, 36 tracts were used to construct the TGC for each hemisphere (29 unilateral and 7 commissural tracts).

We calculated the TGC for each participant in two large datasets, including the Human Connectome Project (HCP) dataset ($n = 968$)²⁴ and IMAGEN dataset ($n = 661$)²⁵. For each participant, the tract reachability map of each tract was reconstructed using 200 decomposed eigenmodes via a general linear model (GLM; Fig. S2), and reconstruction accuracy was assessed by the Pearson correlation coefficient between the empirical and reconstructed maps. We observed high reconstruction accuracy in both datasets. The median reconstruction accuracy for each tract across all participants consistently exceeded 0.8, indicating that the tract reachability map could be precisely reconstructed for each tract (Fig. 2A). To further assess the significance of these reconstructions, we generated null models by spatially rotating the eigenmodes using two independent methods, i.e., BrainSMASH²⁶ and eigenstrapping²⁷. Across 1000 surrogate maps, reconstruction accuracy was significantly lower than when using the actual eigenmodes (Fig. S3). To provide an intuitive understanding of reconstruction performance, we also included visual examples of reconstructed tract reachability maps for four representative association tracts with important functional significance, the three sub-tracts of the superior longitudinal fasciculus (SLF_I, SLF_II, SLF_III) and the arcuate fasciculus (AF), in a representative HCP participant. In the HCP dataset, we observed that the reconstructed tract reachability maps of these four white matter tracts closely matched the actual anatomical projections (Fig. 2B).

We next examined the impact of including varying numbers of eigenmodes on the reconstruction accuracy. As expected, accuracy increased with the number of eigenmodes, with $r = 0.5$ reached using the first 10 eigenmodes and $r > 0.7$ with the first 50 eigenmodes (Fig. S4A). The reconstruction accuracy asymptotically became stable when reaching the first 200 eigenmodes (Fig. S4B). Therefore, we selected the first 200 eigenmodes for the reconstruction throughout this study.

We additionally confirmed that the reconstruction accuracy was not affected by using either the eigenmodes derived from the population-averaged surface or those derived from the individual surfaces. Accuracy remained high when using individual-specific geometric eigenmodes (Fig. S5A). Meanwhile, TGC computed using individual eigenmodes was highly similar to that computed using group-level eigenmodes (Fig. S5B), leading us to use the latter for subsequent analyses. Moreover, although the eigenmodes were computed separately for each hemisphere, the reconstruction accuracy in the right hemisphere also remained high when using 200 eigenmodes (Pearson $r > 0.8$ for all tracts; Fig. S6). Moreover, TGC was calculated based on datasets balanced for gender, ensuring that analyses were performed simultaneously on male and female participants to reduce potential gender-related biases.

TGC exhibits high test-retest reliability and individual specificity

To explore the test-retest reliability of TGC, which guarantees the further application of TGC, we adopted the HCP test-retest dataset ($n = 44$), in which participants underwent the same scanning on separate days. We found that TGC showed high test-retest reliability (all $r > 0.96$; see one example participant in Fig. 2C). That is, for each participant, Pearson correlation coefficient between the TGC from the two scans was higher than 0.96.

Validating the individual specificity of TGC was another important step in further exploring its biological implication. Therefore, we examined whether TGC was capable of identifying individuals in a test-retest scenario. Specifically, we measured the similarity between each pair of subjects across the two scans in the HCP test-retest dataset²⁸. For each participant from the first scan, we computed the

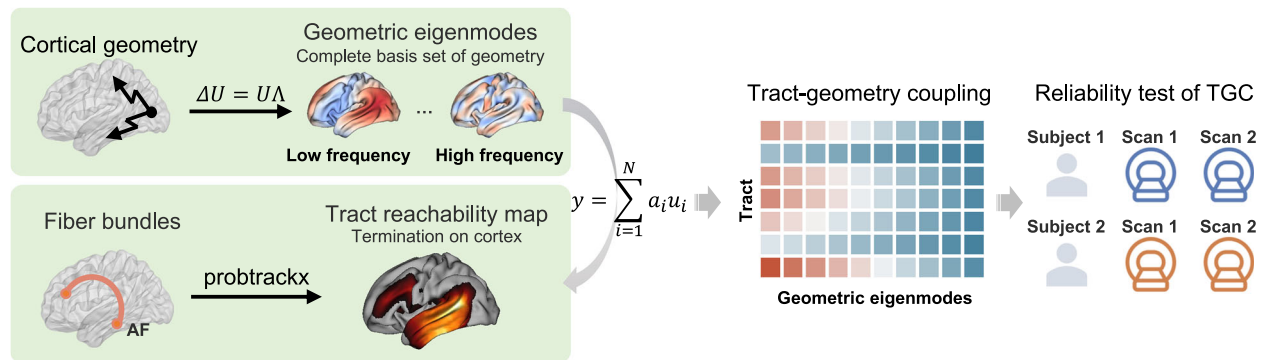
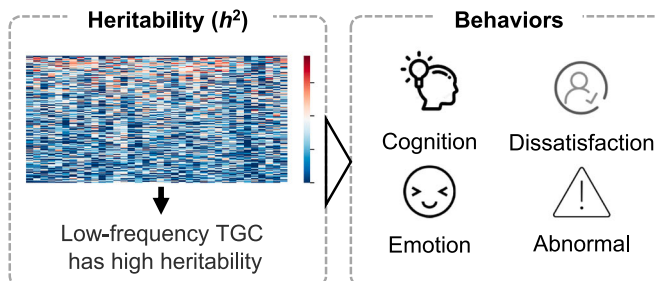
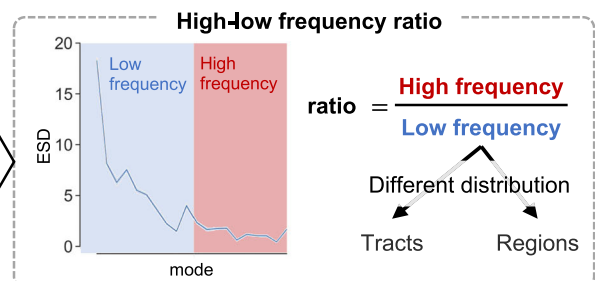
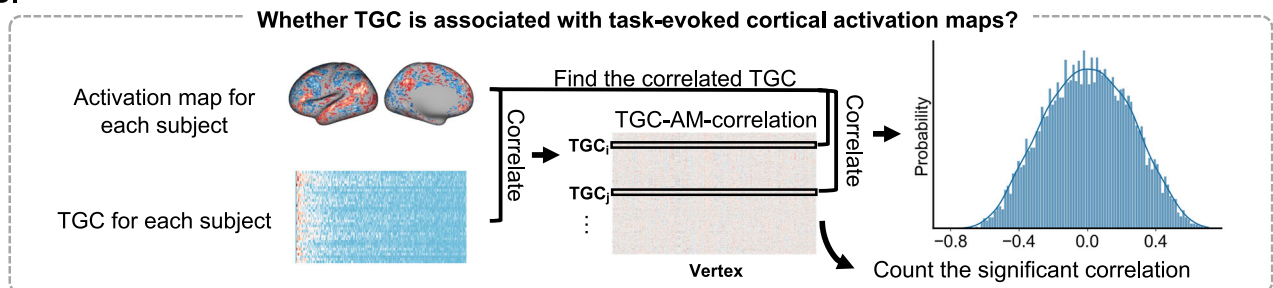
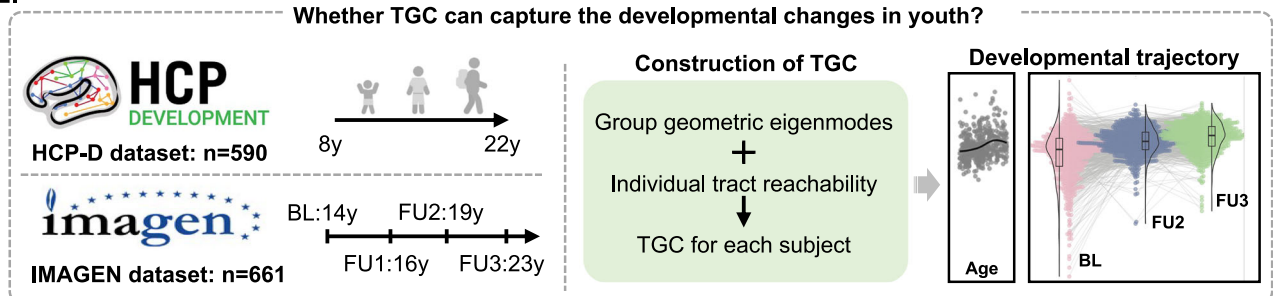
A. Definition of tract-geometry coupling (TGC)**B. Heritability and behavioral relevance of TGC****C. High-low frequency ratio of TGC****D.****E.**

Fig. 1 | Overview of the study. **A** Definition and reliability test of tract-geometry coupling (TGC). Left: We defined TGC to quantify the relationship between cortical geometry and tract reachability. Right: TGC was shown to be stable and to capture individual-specific traits. **B** Heritability and behavioral relevance of TGC. We assessed the heritability of TGC and its behavioral predictability. **C** High-low frequency ratio of TGC and its distribution across regions and tracts. We obtained the high-low frequency ratio of TGC by splitting the spectrum into high and low

portions with equal signal energy based on average energy spectral density (ESD). **D** Functional association of TGC. We used task activation maps (AM) to explore the functional relevance of TGC scores. **E** Developmental trajectory of TGC. Using the HCP-D dataset, we charted developmental pattern from age 8 to 22 and validated these trends using the IMAGEN dataset, which included participants at baseline (BL) at 14 y and follow-up (FU) at 16 y, 19 y, and 23 y. Brain maps in (**A**, **D**) were visualized using BrainSpace and Connectome Workbench.

Pearson correlation coefficient between their TGC and that of every subject in the second scan. If the coefficient for the correct subject was greater than the maximum coefficient for all other subjects, the identity of that subject was predicted. We found that TGC could correctly identify all subjects (identification accuracy [IA] = 100%), indicating its strong individual specificity (Fig. 2D, left). We repeated

the same procedure using the TGC of each tract separately and found that all tracts performed well in individual identification, except for four white matter tracts having IA < 95% (uncinate fasciculus [UF]: IA = 93%, striato-fronto-orbital tract [ST_FO]: IA = 84%, corpus callosum rostrum [CC_1]: IA = 82%, corpus callosum anterior midbody [CC_4]: IA = 86%; Fig. 2D, right).

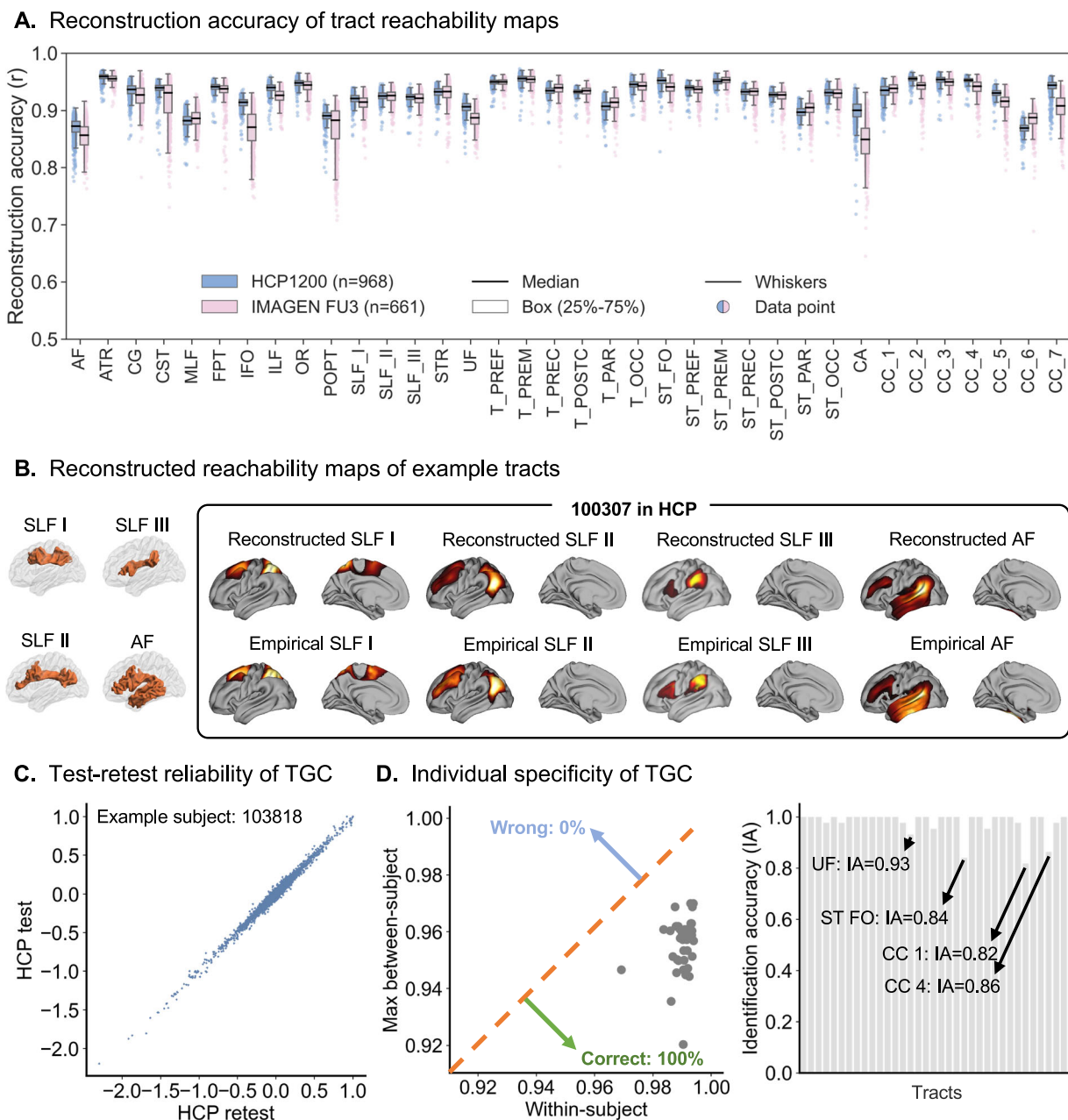


Fig. 2 | Characterization of TGC. A Reconstruction accuracy of tract reachability maps for the HCP ($n = 968$) and IMAGEN FU3 ($n = 661$) datasets. For each tract, the center line of the box plot indicates the median correlation coefficient (r) between empirical and reconstructed reachability maps across participants. The box edges represent the interquartile range (25th–75th percentiles), whiskers denote the data range within 1.5×inter quartile range (IQR), and individual data points are overlaid with the median marked by a central line (blue for HCP1200, pink for IMAGEN). All tracts showed median reconstruction accuracy above 0.8. **B** Empirical and reconstructed reachability maps for several example tracts. **C** TGC exhibits high test-retest reliability. The similarity of TGC between two scans of the same subject was high. One representative participant was shown here, $r = 0.99$. **D** Left: TGC

successfully captured individual differences and predicted the identities of all subjects (identification accuracy [IA] = 100%) in the HCP dataset. Points above the diagonal indicate incorrect individual identification, while points below the diagonal indicate correct identification. Right: The identification accuracy based on TGC of each tract. SLF_I superior longitudinal fasciculus I, SLF_II superior longitudinal fasciculus II, SLF_III superior longitudinal fasciculus III, AF arcuate fasciculus, UF uncinate fasciculus, ST_FO striato-fronto-orbital tract, CC_1 corpus callosum rostrum, CC_4 corpus callosum anterior midbody. Tract and brain maps in (B) were visualized using BrainNet Viewer and Connectome Workbench, respectively. Source data are provided as a Source Data file.

The contribution of eigenmodes to TGC is frequency-related

As the eigenmodes correspond to spatial frequencies, we wanted to examine the different contributions of high- and low-frequency eigenmodes. Following Preti et al.²⁹, we decomposed the tract reachability maps into two components: one closely coupled with geometry, y^l , represented by low-frequency eigenmodes, and another less closely coupled, y^h , represented by high-frequency eigenmodes (Fig. S7). We found a stronger coupling relationship in the low-frequency

eigenmodes, while a weaker relationship was observed in the high-frequency eigenmodes (Fig. 3A, B), suggesting that high-frequency eigenmodes may capture individual differences in the coupling between cortical geometry and connectivity. This motivated us to evaluate TGC heritability using twins from the HCP dataset ($n = 388$, 102 monozygotic and 92 dizygotic pairs). We found that low-frequency eigenmodes showed higher TGC heritability than high-frequency eigenmodes ($r = -0.74$, $p = 2e-35$; Fig. 3C, left). This difference was

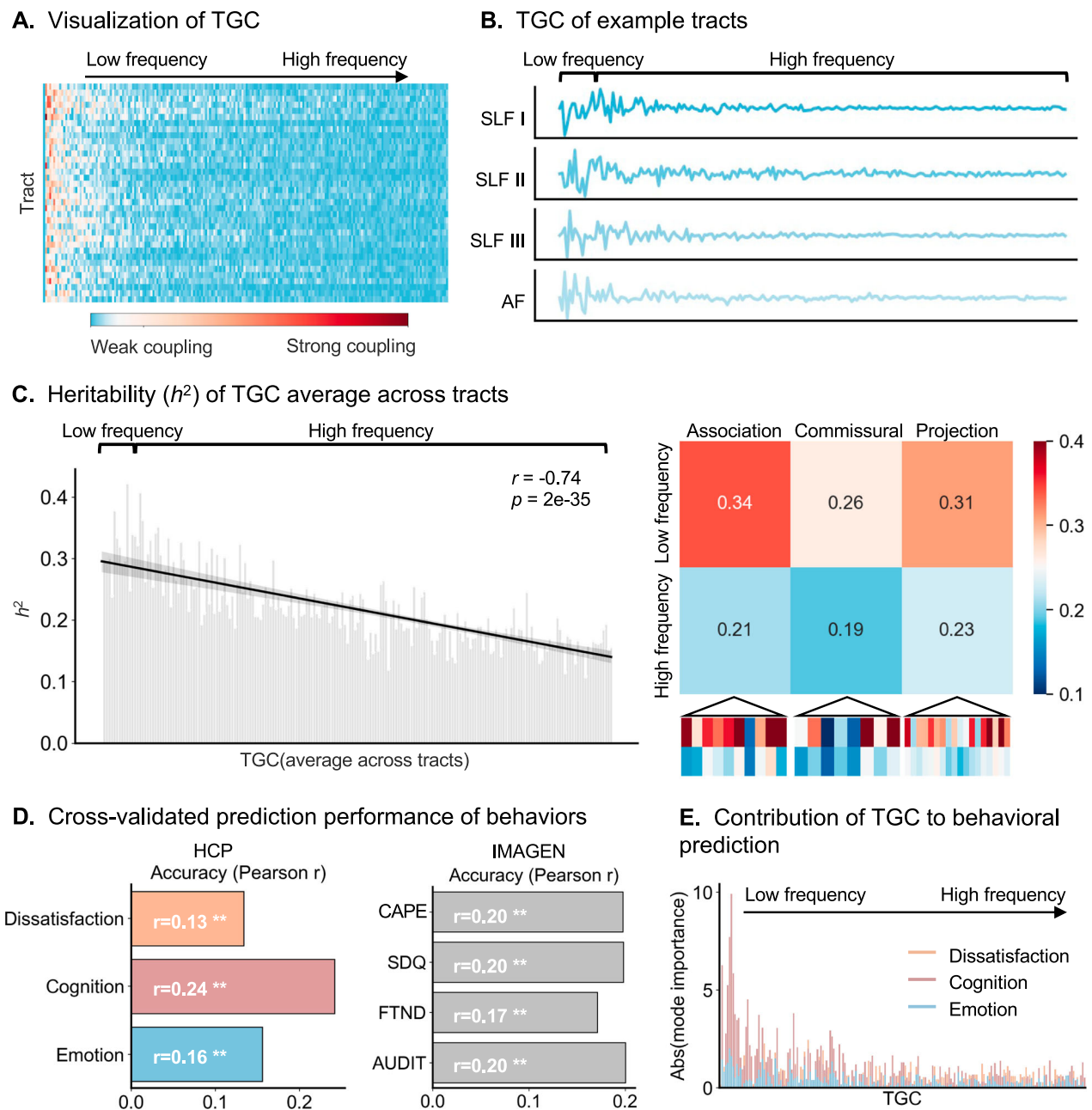


Fig. 3 | Heritability and behavioral relevance of TGC. **A** Visualization of TGC. A stronger coupling relationship was observed in the low-frequency eigenmodes, while a weaker relationship was found in the high-frequency eigenmodes. **B** TGC for several example tracts. **C** Left: Heritability of TGC. Coupling between tracts and low-frequency eigenmodes exhibited greater heritability than coupling with high-frequency eigenmodes. Right: Differences in heritability between low- and high-frequency coupling were also observed across different tract types. Pearson correlation was performed between the frequency and the heritability, and the two-tailed p -value obtained was provided. The black line represents the fitted linear regression. The surrounding shaded band denotes the 95% confidence interval, indicating the range in which the true regression line is expected to fall with 95% probability. **D** TGC predicted the three behavior-derived components in the HCP

dataset (dissatisfaction: $r = 0.13$, $p_{\text{permutation}} < 0.01$; cognition: $r = 0.24$, $p_{\text{permutation}} < 0.01$; emotion: $r = 0.16$, $p_{\text{permutation}} < 0.01$, FDR corrected), as well as four dysfunctional behavior measures in the IMAGEN dataset (Community Assessment of Psychic Experiences [CAPE]: $r = 0.20$, $p_{\text{permutation}} < 0.01$; Strengths and Difficulties Questionnaires [SDQ]: $r = 0.20$, $p_{\text{permutation}} < 0.01$; Fagerstrom Test for Nicotine Dependence [FTND]: $r = 0.17$, $p_{\text{permutation}} < 0.01$; Alcohol Use Disorders Identification Test [AUDIT]: $r = 0.20$, $p_{\text{permutation}} < 0.01$, FDR corrected). The two-tailed p -values were obtained from 1,000 permutation tests by comparing the observed correlation to the distribution of permuted values. $^{**}p < 0.01$. **E** Contribution of TGC to behavioral predictions. Low-frequency TGC contributed more strongly to all three behavioral components. Source data are provided as a Source Data file.

also observed in the association, commissural, and projection tracts (Fig. 3C, right). The observed higher heritability of low-frequency TGC suggests that genetic factors have a stronger influence on the coupling between white matter tracts and large-scale, low-frequency geometric patterns, while the lower heritability of high-frequency TGC may reflect a greater influence of environmental factors, experience-

dependent plasticity, and fine-scale individual variations. In other words, the genetic factors firstly establish the global architecture of white matter-cortex coupling, while environmental influences gradually refine and modulate the high-frequency, fine-grained connectivity patterns throughout development and adulthood. This dual influence could underpin individual differences in cognitive and behavioral

traits, further inspiring us to explore how TGC might predict behavioral performance and the specific contributions of different eigenmode frequencies to this prediction.

To test whether TGC could predict behavior at the individual level and whether predictive performance was related to eigenmode frequency, we used kernel ridge regression (KRR) to predict the behavioral scores in the HCP dataset. To enhance prediction robustness and efficiency, we first conducted principal component analysis (PCA) on the 58 behavioral measures³⁰, and focused on the first three principal components, which broadly represented cognitive, emotional, and dissatisfaction domains³¹. We found that the three behavioral components could be well predicted (dissatisfaction: $r=0.13$, $p_{\text{permutation}} < 0.01$; cognition: $r=0.24$, $p_{\text{permutation}} < 0.01$; emotion: $r=0.16$, $p_{\text{permutation}} < 0.01$, FDR corrected; Fig. 3D, left, Fig. S8). To provide a comprehensive assessment of the TGC's predictive performance, we also reported prediction results for each of the 58 individual behavioral measures in Supplementary Data 1.

To investigate the contribution of different types of eigenmodes and tracts, we calculated feature contributions using the Haufe transformation³², resulting in a (*eigenmodes* \times *tracts*) matrix. Aggregating the TGC contribution across all tracts, we found that low-frequency TGCs were the most informative for behavior prediction (Fig. 3E). When investigating the contributing tracts, we found that dissatisfaction was positively related to corpus callosum splenium (CC_7), anterior thalamic radiation (ATR), and SLF_II and negatively related to corpus callosum rostral body (CC_3), commissure anterior (CA), and thalamo-premotor tract (T_PREM). Cognition was positively related to CC_3, SLF_I, and corpus callosum isthmus (CC_6) and negatively related to CC_4, striato-precentral tract (ST_PREC), and thalamo-prefrontal tract (T_PREF). Emotion was positively related to corpus callosum genu (CC_2), SLF_I, and superior thalamic radiation (STR) and negatively related to CA, striato-postcentral tract (ST_POSTC), and inferior longitudinal fasciculus (ILF; Fig. S9). Taking cognition as an example, CC_3 and SLF_I, which connect the frontal lobe, contributed more, highlighting the critical role of the frontal lobe in cognitive behaviors³³. Additionally, the posterior parietal and visual networks targeted by CC_6 are also known to support cognitive functions³⁴.

We also showed that TGC could predict high-risk behaviors using KRR on the IMAGEN data. The results again demonstrated its ability to reflect functionally abnormal behaviors (CAPE: $r=0.20$, $p_{\text{permutation}} < 0.01$; SDQ: $r=0.20$, $p_{\text{permutation}} < 0.01$; FTND: $r=0.17$, $p_{\text{permutation}} < 0.01$; AUDIT: $r=0.20$, $p_{\text{permutation}} < 0.01$, FDR corrected; Fig. 3D, right, Fig. S8, Supplementary Data 1) and psychopathology symptoms (depband: $r=0.13$, $p_{\text{permutation}} < 0.05$; sphband: $r=0.22$, $p_{\text{permutation}} < 0.01$; dcgena: $r=0.23$, $p_{\text{permutation}} < 0.01$; ocdband: $r=0.19$, $p_{\text{permutation}} < 0.01$; eatband: $r=0.19$, $p_{\text{permutation}} < 0.01$; ptsdband: $r=0.15$, $p_{\text{permutation}} < 0.05$, FDR corrected; Figs. S10, S8, Supplementary Data 1). These findings suggest that the decoupling between white matter tracts and cortical geometry is closely linked to functional impairments. The contributing traits to these behaviors were shown in Figs. S11, S12.

Tract reachability was also used to predict behaviors, and its performance was compared to that of TGC. Both TGC and tract reachability could predict cognitive behaviors in the IMAGEN dataset, with TGC showing better performance (Fig. S13). These results highlight the TGC's close functional relevance, as it acts as a bridge that links the white matter and the cortical geometry. Notably, TGC also exhibited longitudinal predicted ability. We found that in the IMAGEN cohort, TGC at age 14 was able to predict the cognitive scores at ages 19 and 23. This suggests that TGC can capture the developmental changes, serving as a foundation for cognitive maturation across adolescence. Behaviors in the HCP and IMAGEN datasets could also be significantly predicted using TGC in the right hemisphere (Supplementary Data 1), highlighting the individual variability of TGC in the right hemisphere and its functional associations.

A high-low frequency ratio shows functional relevance

Given the finding of a stronger coupling relationship between white matter tracts and low-frequency eigenmodes than high-frequency eigenmodes, we sought to provide a quantitative measure of this difference, i.e., the high-low frequency ratio. Using tract reachability maps that were separated into two components represented by high- and low-frequency eigenmodes (y^H and y^L), we calculated the ratio between the norm of y^H and y^L for each tract as a measure of tract-geometry coupling. We then calculated the high-low frequency ratio for each tract and assessed the difference across association, commissural, and projection tracts. A significant difference was found between association and projection tracts (HCP: $t=3.50$, $p < 0.005$; IMAGEN-FU3: $t=2.92$, $p < 0.01$; Supplementary Data 2). As conservative fiber pathways, projection tracts, such as thalamic-cortical projection tracts, showed stronger coupling with large-scale low-frequency geometric eigenmodes. In contrast, association tracts, which are closely linked to complex cognitive functions, exhibited a larger influence from high-frequency eigenmodes, which showed lower heritability, suggesting that they are more susceptible to environmental influences.

We averaged the high-low frequency ratio map across tracts, resulting in an average map (Fig. 4A). We assigned this map to the multimodal parcellation scheme³⁵ and found that regions showing a high high-low frequency ratio included the dorsolateral prefrontal cortex, inferior parietal lobule, rostroventral insula, and cingulate cortex (Fig. 4A), which are components of the multiple demand network³⁶ and the default mode network³⁷. Similar results were replicated in the FU3 cohort from the IMAGEN dataset ($r=0.91$, $p=3e-68$; Fig. 4B) and using another atlas, the Brainnetome parcellation³⁸ (Fig. S14).

When investigating the specific white matter tracts connected to these subregions, we found that low-ratio regions were associated with the ILF, AF, cingulum (CG), and SLF_III, while high-ratio regions were associated with the STR, SLF_I, striato-premotor tract (ST_PREM), and UF (Fig. 4C). As the coupling between tracts and low-frequency eigenmodes was more influenced by genetic factors, we hypothesized that individualized and local information was more prevalent in the coupling with high-frequency eigenmodes. This might be reflected in the functional association of the high-low frequency ratio. Functional decoding using NeuroSynth³⁹ showed that regions with a high ratio were related to "intention", "arithmetic", "saccade", and "belief", whereas regions with a low ratio were associated with "voluntary", "motor", "movement", and "sensorimotor" (Fig. 4D).

We also explored the potential biological implications of high-low frequency ratio by estimating its relationship to various neurobiological brain maps^{40,41}. The high-low frequency ratio map demonstrated significant correlations with MEG-derived power maps across different frequencies ($r_{\text{megbeta}}=0.42$, $p_{\text{megbeta}} < 0.01$; $r_{\text{meggamma1}}=0.35$, $p_{\text{meggamma1}} < 0.01$; $r_{\text{megtheta}}=0.35$, $p_{\text{megtheta}} < 0.01$; $r_{\text{megalpha}}=-0.3$, $p_{\text{megalpha}} < 0.01$, FDR corrected), the second gradient of functional connectivity ($r=-0.27$, $p < 0.01$, FDR corrected), and the cerebral blood flow (CBF) map ($r=0.23$, $p < 0.05$, FDR corrected; Fig. S15, left). Additionally, we tested a total of 19 receptor maps obtained from autoradiography and in vivo PET imaging⁴⁰. These maps include the distributions of major neurotransmitter systems, such as dopamine and serotonin, among others, providing a comprehensive overview of the neurochemical architecture of the human cortex. The ratio map showed significant associations with seven receptor maps, including MU, CBI, A4B2, H3, SHT2a, VACHT, and DAT ($r_{\text{MU_carfentanil}}=0.31$, $p_{\text{MU_carfentanil}} < 0.01$; $r_{\text{CBI}}=0.29$, $p_{\text{CBI}} < 0.01$; $r_{\text{A4B2}}=0.28$, $p_{\text{A4B2}} < 0.01$; $r_{\text{H3}}=0.28$, $p_{\text{H3}} < 0.01$; $r_{\text{SHT2a_mdl}}=-0.27$, $p_{\text{SHT2a_mdl}} < 0.01$; $r_{\text{VACHT}}=0.26$, $p_{\text{VACHT}} < 0.01$; $r_{\text{DAT}}=0.24$, $p_{\text{DAT}} < 0.05$, FDR corrected; Fig. S15, right), highlighting specific neurochemical contributions to the observed white matter-cortical coupling patterns.

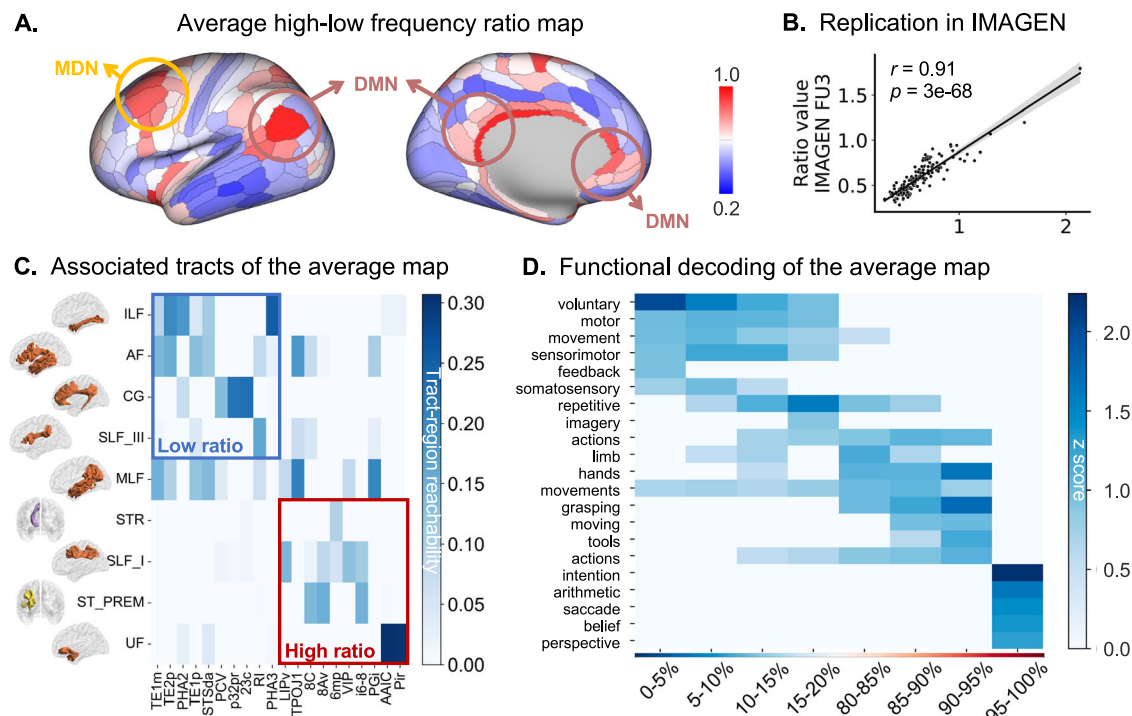


Fig. 4 | High-low frequency ratio of TGC. A Average high-low frequency ratio map across tracts. Regions with higher ratios are located in the dorsolateral prefrontal cortex, inferior parietal lobule, rostromedial insula, and cingulate cortex, which are part of the multiple demand network (MDN) and default mode network (DMN). **B** Replication using the FU3 cohort from the IMAGEN dataset ($r = 0.91$, $p = 3e-68$). Black line: linear regression fit; shaded area: 95% confidence interval, indicating the range within which the true regression line is expected to lie with 95% probability. The two-tailed p -value obtained was provided. **C** Associated tracts for cortical regions with high and low ratio values. The x-axis represents the top 10 regions with

the highest and lowest ratio values, and the corresponding tracts associated with these regions. **D** Functional decoding of the average high-low frequency ratio map. ILF inferior longitudinal fasciculus, AF arcuate fasciculus, CG cingulum, SLF_III superior longitudinal fasciculus III, MLF middle longitudinal fasciculus, STR striatum, SLF_I superior longitudinal fasciculus I, ST_PREM striato-premotor tract, UF uncinate fasciculus. Brain maps in (A) were visualized using Connectome Workbench and tract maps in (C) were visualized using BrainNet Viewer. Source data are provided as a Source Data file.

TGC reproduces the task-evoked brain activation pattern

To more directly test the connection between TGC and the brain functions, we next investigated whether TGC is associated with task-evoked cortical activation maps derived from fMRI. We used task activation maps from 47 contrasts in the HCP dataset. For each contrast, we correlated each TGC with each cortical vertex across subjects, resulting in a correlation matrix, which was then correlated with the activation map, yielding a correlation for each activation map. We found that the maximum correlation between the TGC and the activation map (TGC-AM-correlation) closely resembled the activation map itself (Figs. 5A, S16). For example, a stronger correlation was found in the posterior part of the inferior parietal lobule, which is also the peak activation location of the contrast map for Language Story-Math (Fig. 5A, left). This suggests that the variation trend of TGC across the population corresponds to the trend of activation intensity across the population, especially at significantly activated vertex. This observation was further validated by calculating the relationship between the activation value of an example vertex and the TGC across subjects (Fig. 5B). These results indicate that the association between TGC and the activation map is continuously and uniformly distributed across subjects, rather than being coincidental or driven by a few individuals with exceptionally high TGC and activation values.

We then quantified the significance of the correlation by performing multiple comparisons on the correlation matrix described above and counting the number of vertices showing significant correlation values for each TGC. The similarity between activation maps for contrasts within the same behavioral domain was high (Fig. S17), indicating that TGC captures functional information relevant to task activation domains.

Development of TGC during youth

Since understanding the structural coupling between gray matter and white matter is crucial for comprehending brain development and its relation to cognitive functions, and TGC has shown its potential in this regard, we further explored its relevance by delving into its developmental trajectory during childhood and adolescence. We used data from Human Connectome Project in Development (HCP-D) ($n = 590$) and IMAGEN ($n = 661$) datasets to investigate the developmental trajectory of TGC. The same methodology was applied to construct TGC in both datasets. We first used cross-sectional data from the HCP-D dataset to establish the developmental trajectory of the TGC L1-norm value for each tract using a generalized additive model (GAM), showing that the development of most tracts was significantly related to age (Fig. 6A). The tracts were sorted by the rate of increase, represented by the first derivative of the GAM (Fig. 6A, inset), and exhibited significant differences across tract types (Mann-Whitney U test: $p_{\text{association-commissural}} = 5.8e-04$; $p_{\text{association-projection}} = 4.4e-05$; $p_{\text{commissural-projection}} = 0.45$; Fig. 6A, inset). This suggests that tracts with higher L1-norm values, reflecting stronger coupling with geometry, demonstrate greater increases with age.

Figure 6B presents six example tracts. The left column of each subfigure illustrates the developmental trajectories derived from the HCP-D dataset, while the right column displays the corresponding validation using the IMAGEN longitudinal dataset. In the IMAGEN dataset, pair t-tests were performed between each pair of time points. The TGC of all six tracts in FU2 was consistently higher than in BL. Interestingly, tracts associated with language functions, such as the UF, middle longitudinal fasciculus (MLF), and AF, exhibited growth starting around age 14 and peaking around age 19.

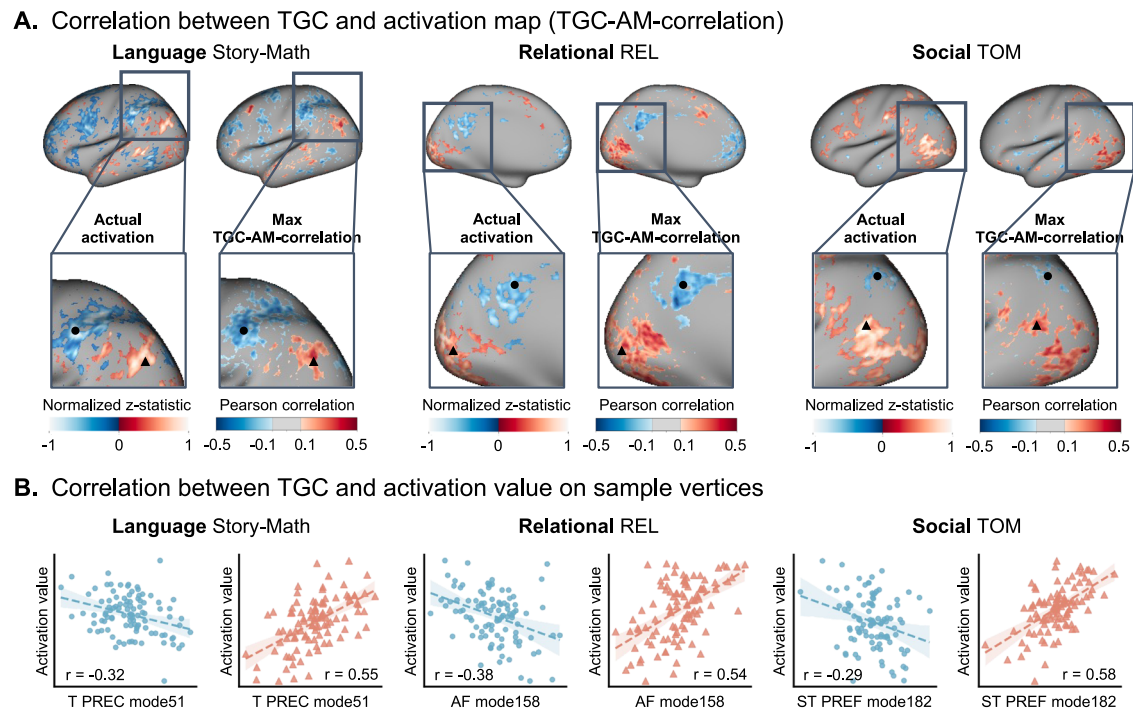


Fig. 5 | TGC represented functional association. **A** The maximum correlation between TGC and the activation map (TGC-AM-correlation) closely resembled the actual activation pattern. For example, a stronger correlation was observed in the posterior part of the inferior parietal lobule, also corresponds to the peak activation location in the Language Story-Math contrast map. **B** The activation value at a specific vertex showed a significant correlation with TGC across subjects. The vertex marked by the black circle in **(A)** was negatively correlated with TGC,

whereas the vertex marked by the black triangle in **(A)** was positively correlated with TGC. REL relational, TOM theory of mind, T_PREC thalamo-precentral tract, AF arcuate fasciculus, ST_PREF striato-prefrontal tract. Blue/red line: linear regression fit; shaded area: 95% confidence interval. The two-tailed p -values obtained were provided. Brain maps in **(A)** were visualized using Connectome Workbench. Source data are provided as a Source Data file.

Furthermore, we analyzed the age effect for each TGC and found that most TGC exhibited significant developmental changes (Fig. S18A). These changes were consistently observed in both the HCP-D and IMAGEN datasets (Fig. S18B), further highlighting that TGC can capture developmental changes and reflect heterogeneity across different tracts.

Discussion

The present study addressed a critical yet underexplored question of how cortical geometry and white matter tracts, two fundamental and interconnected aspects of brain structure, are coupled. By introducing TGC, we quantified this relationship, integrating recent advances in cortical geometry decomposition²¹ and white matter tract segmentation^{22,23}. TGC was well-validated in the current study, showing high test-retest ability and individual specificity. These results are not influenced by the gender of the participants, as we ensured a balanced representation of genders in all analyses. We further analyzed the frequency-related contributions of eigenmodes to TGC, finding that the low-frequency eigenmodes, which correspond to long-wavelength signals in the brain²¹, exhibited higher contributions. Moreover, TGC demonstrated significant predictive ability for a range of individual behaviors, extending the conventional brain-behavior paradigm to include the coupling between cortical geometry and white matter tracts. Furthermore, we demonstrated that TGC well reproduced the task-evoked brain activation patterns, indicating that the strength of coupling was functionally relevant and potentially affected task-specific brain dynamics. Developmental analyses further revealed distinct age-related trajectories in TGC from childhood to adolescence, underscoring the interplay between cortical geometry and white matter organization throughout neurodevelopment. Taken together, our findings not only introduced a robust methodological

framework for quantifying the coupling between cortical geometry and white matter tracts but also emphasized their integrative role in shaping brain function and behavior. By simultaneously examining these two interconnected aspects of the brain, we provided a consolidated step forward in bridging the gap between cortical surface geometry and its underlying white matter architecture.

Previous studies have focused on region-to-region connectivity but have overlooked the influence of white matter on these regions, which are physically embedded in three-dimensional space and manifest complex geometric shapes. This gap motivates us to consider the mutual constraints between cortical geometry and white matter pathways, aiding our understanding of how the brain's architecture gives rise to cognition and behavior^{3,21}. A hypothesis about the formation of geometric patterns in gray matter is supposed to be related to the tension from the underlying white matter, which also constrains the direction and range of axonal growth^{9,10}. This process begins during the fetal period⁴² and continues to evolve through childhood and adolescence^{43,44}. This phenomenon could be explained by synaptic construction, increased axonal diameter, and myelination at the microstructural level, as indicated by physical-mechanical models, lesion studies, and molecular experiments^{45,46}. However, studying associations of a single brain region has its limitations. Therefore, we proposed to characterize the coupling relationship between tract connectivity and cortical geometry from a global and macroscale perspective. Tract reachability, characterized using connectivity blueprints that help mitigate bias to some extent when fiber bundle enters the gray matter, provides a comprehensive description of tract-to-cortex connectivity^{23,47}. We provided clear evidence that tract reachability was preferentially expressed using low-frequency, smooth spatial patterns obtained from the harmonic decomposition of cortical geometry. In addition to the highly repeatable observations of this

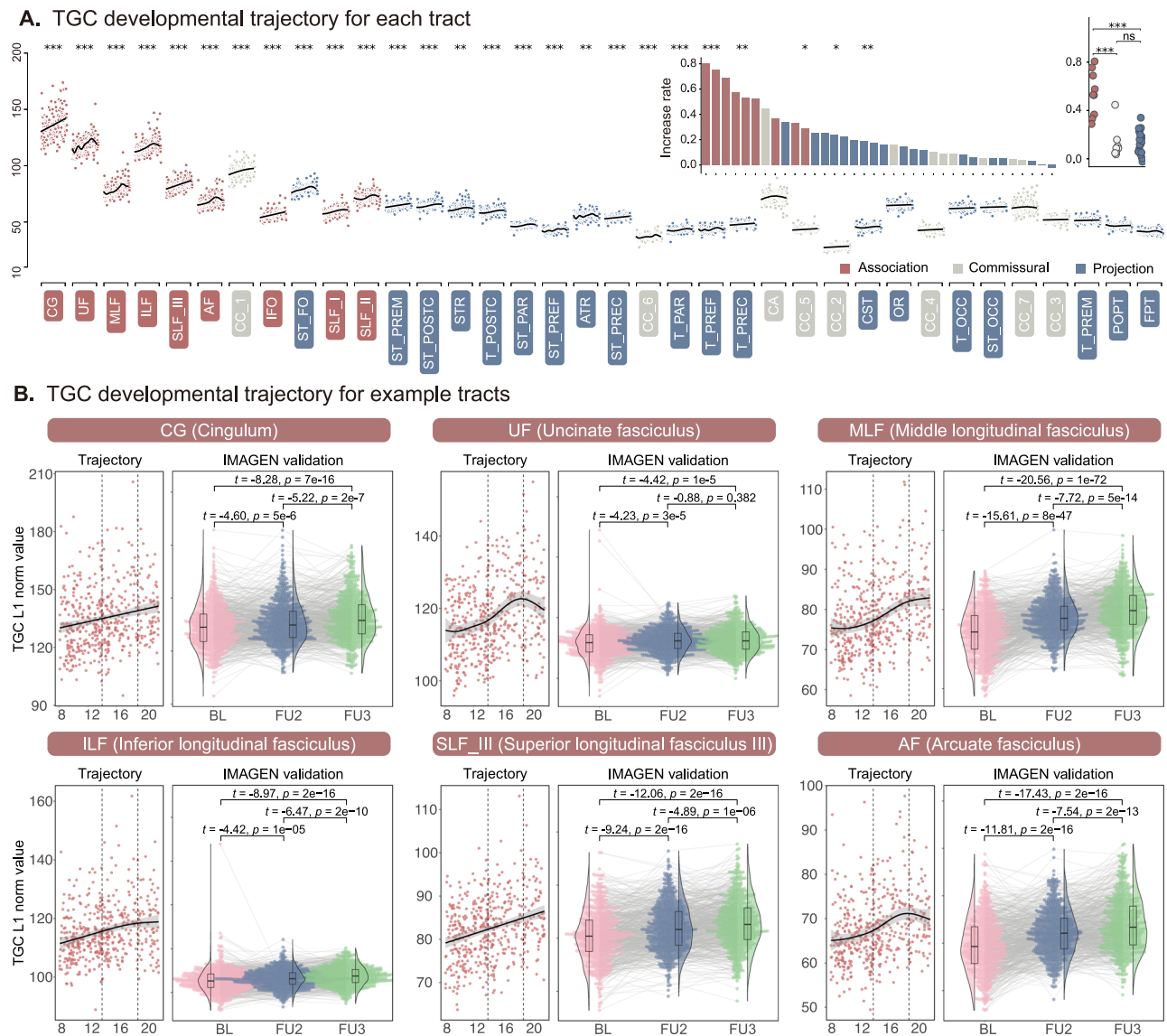


Fig. 6 | Developmental trajectory of TGC. A The HCP-D dataset was used to calculate the developmental trajectory of the TGC L1-norm value ($n = 590$; age range, 8–22). GAM results are shown for each tract. The increase rate of each tract was calculated as the first derivative of the GAM age spline curve. Significant differences were observed by the Mann-Whitney U test between each two tract types, with the two-tailed p -values provided in the corresponding panels (association vs. commissural: $p = 5.759 \times 10^{-4}$; commissural vs. projection: $p = 0.4493$; association vs. projection: $p = 4.447 \times 10^{-5}$). *** $p < 0.001$, ** $p < 0.01$, * $p < 0.05$. **B** Developmental trajectory of six example tracts. Left in each subfigure: Detailed developmental trajectories of the top six example tracts. Shade regions indicate 95% confidence

intervals. Two black dotted lines denote age 14 and 19. Right: TGC L1-norm value for the same tracts at age 14, 19, and 23 in the IMAGEN dataset. Each dot represents an individual, with gray lines connecting repeated measures from the same participant. Half-violin plots display the kernel density of the data distribution. Boxplots within each violin plot show the median (center line), interquartile range (IQR) (box edges). Pair t-test were performed between each pair of ages, with t -values and two-tailed p -values indicated. CG cingulum, UF uncinate fasciculus, MLF middle longitudinal fasciculus, ILF inferior longitudinal fasciculus, SLF_III superior longitudinal fasciculus III, AF arcuate fasciculus. Source data are provided as a Source Data file.

coupling across different cohorts, we demonstrated both stability and uniqueness in each subject, as well as individual predictability for cognitive and high-risk abnormal behaviors. These findings suggest that tract-geometry coupling is a reliable indicator of the relationship between cortical geometry and white matter connectivity.

The coupling relationship between white matter tracts and cortical geometric patterns undergoes rapid changes during fetal development, while also dynamically evolving and adjusting during childhood and adolescence^{43,44}. For example, in children and adolescents, a significant association has been observed between the rate of cortical thickness reduction and the rate of fractional anisotropy increase in the local gyral regions of the frontal lobe⁴⁸. The maturation of cortical regions is influenced by the white matter tracts, where

structurally connected areas share similar cytoarchitecture^{49–51}, neurotransmitter receptor profiles⁴⁰, and exhibit coordinated development through interregional communication and spontaneous neuronal activity coupling⁵². Our results demonstrate that the coupling between most white matter tracts and cortical geometry evolves dynamically throughout development. White matter tracts with significant developmental patterns show stronger coupling with cortical geometric structures during normal development. Notably, language-related tracts such as the AF, MLF, and UF exhibit both high coupling values and rapid rates of increase. These tracts play a critical role in the structural connectivity underlying several cognitive functions, including language processing^{53–55}. The observed stronger coupling in these tracts likely reflects the intricate co-development of cortical

regions and white matter pathways essential for linguistic and executive functions. Furthermore, aberrant coupling of these tracts during adolescence—a period of heightened brain plasticity—has been linked to disorders such as schizophrenia and depression, which often involve impairments in language processing, emotional regulation, and cognitive control^{56–58}. In our analysis, we also demonstrated significant predictive associations between TGC and psychotic-like symptoms, such as CAPE, cognitive impairments (SDQ), and addictive behaviors. Investigating the developmental trajectories and coupling relationships of these tracts provides valuable insights into their functional significance. Understanding how these patterns deviate in neurodevelopmental disorders could help guide interventions aimed at reducing functional impairments and improving outcomes for affected individuals.

From the visualization of various cortical geometric eigenmodes, the low-frequency components showed typical anterior-posterior and dorsal-ventral patterns, with clear separations across different brain lobes. As frequency increased, more refined brain regions or networks, including the insula, default mode network, and motor areas, became increasingly distinct. Additionally, we found higher heritability in the coupling between low-frequency eigenmodes and white matter tracts compared to high-frequency eigenmodes. This could be explained by morphogens that guide axons along the dorsal-ventral, rostral-caudal, and lateral-medial axes during early development, which aligns with the low-frequency geometric eigenmodes and contribute to the functional arealization of the cerebral cortex in adults⁵⁹. This process further leads to varying functional significance across different cortical areas. In addition, higher heritability was found in projection tracts, consistent with their conserved roles across subjects during phylogenesis and ontogenesis^{60,61}. In contrast, individual differences in cortical structure and functions were more pronounced in the high-frequency components, which influence the connectional patterns of association tracts^{2,62}.

In a recent study, Pang et al. constructed a more compact and accurate macroscopic expression of brain function based on the geometric basis of the cerebral cortex²¹ and captured the fundamental anatomical constraints of brain dynamics. White matter networks support the realization of brain functions and promote effective and coordinated information transmission, including both spontaneous and evoked brain activity across regions^{3,63–65}, while also providing a basis for the functional dynamics of the brain through modern biophysical models and network control theory^{66–69}. In this study, the coupling between cortical geometry and tract reachability across the entire cortex showed greater decoupling in most of the association cortex, particularly in the multiple demand network and default mode network, which are domain-general in cognitive operations, indicating that high-frequency, short-range, and local geometric eigenmodes interacted more strongly with white matter tracts than low-frequency ones. This consistent relationship is also supported by the predictability of TGC for different aspects of brain functional activations and behaviors. This indicates that TGC could serve as a valuable reference for clinical and functional studies, enabling the investigation of how variations in these connections might relate to neurological and psychiatric conditions, thus supporting the development of diagnostic tools and therapeutic strategies targeting specific white matter pathways.

Several technical and methodological limitations should be acknowledged. The first and most direct issue is the accuracy of using diffusion MRI to map structural connectivity. Gyral bias caused by current reconstruction and tractography methods may lead to false positive results, especially when encountering crossing fibers^{70–72}. In addition, dMRI can only evaluate the microstructure of white matter indirectly and is limited in its ability to describe intra-axial characteristics, especially at lower diffusion weights. This makes it difficult to interpret specific indicators related to development as

precise microstructural events^{73,74}. In our current work, we quantitatively analyzed the coupling relationship between cortical geometric patterns and white matter tract reachability in two adult brain datasets. However, what is even more interesting is how this coupling relationship is formed and evolves during development and evolution. Previous studies have shown that patients with neurodevelopmental disorders exhibit abnormalities in cortical maturation and white matter connectivity^{75,76}. In the future, more attention should be given to studying how this coupling affects these atypical populations.

Methods

Datasets used in present study are open sources and have been approved by their local research ethics committees. Informed consent has been signed by all participants. The current research complies with all relevant ethical regulations as set by the Biomedical Research Ethics Review Committee, Institute of Automation, Chinese Academy of Sciences (study number IA21-2402-020416).

Data acquisition

HCP dataset. We used a publicly available dataset containing 968 subjects (459 males; mean age, 28.70 ± 3.71 ; age range, 22–35) provided by the Human Connectome Project (HCP) dataset²⁴ (<http://www.humanconnectome.org/>). All the scans and data from the individuals included in the study had passed the HCP quality control and assurance standards.

The scanning procedures and acquisition parameters were detailed in previous publications⁷⁷. In brief, T1w images were acquired with a 3D MPRAGE sequence on a Siemens 3 T Skyra scanner equipped with a 32-channel head coil with the following parameters: TR = 2400 ms, TE = 2.14 ms, flip angle = 8°, FOV = 224×320 mm², voxel size = 0.7 mm isotropic. Diffusion data were acquired using single-shot 2D spin-echo multiband echo planar imaging on a Siemens 3 Tesla Skyra system (TR = 5520 ms, TE = 89.5 ms, flip angle = 78°, FOV = 210×180 mm). These consisted of three shells (b -values = 1000, 2000, and 3000 s/mm²), with 90 diffusion directions isotropically distributed among each shell and six $b = 0$ acquisitions within each shell, with a spatial resolution of 1.25 mm isotropic voxels.

IMAGEN dataset. We also included the IMAGEN dataset in our analysis²⁵. IMAGEN is a large-scale longitudinal neuroimaging-genetics cohort study designed to understand the biological basis of individual variability in psychological and behavioral traits and their relationship to common psychiatric disorders. The participants were recruited from schools in France, the UK, Ireland, and Germany. MRI data were acquired at eight IMAGEN assessment sites with 3 T MRI scanners from different manufacturers (Siemens, Philips, GE Healthcare, Bruker). The study involved a thorough neuropsychological, behavioral, clinical, and environmental assessment of each participant. The participants also underwent a biological characterization that included the collection of T1-weighted structural MRI and diffusion MRI data. A more detailed description can be found in the standard operating procedures for the IMAGEN project (<https://imagen-europe.com/resources/standard-operating-procedures/>).

In this investigation, we used T1-weighted structural MRI data, diffusion MRI data, and behavior data from ages 14 (baseline), 19 (follow-up2), and 23 (follow-up3). A total of 661 participants (304 males; mean age, 14.43 ± 0.39 in baseline, 18.97 ± 0.68 in follow-up2, 22.46 ± 0.62 in follow-up3) with complete neuroimage and demographic data (including age, gender, handedness, and acquisition site) were included. The scanning variables were specifically chosen to be compatible with all the scanners. Diffusion imaging protocols were specifically harmonized across sites and scanners for the IMAGEN study, while structural scans were based on the protocols developed by the Alzheimer's Disease Neuroimaging Initiative (ADNI) (<https://>

adni.loni.usc.edu/data-samples/adni-data/neuroimaging/mri/mri-scanner-protocols/), which are optimized to provide very similar results despite differing scanner capabilities and thus differing acquisition parameters.

T1w scans were acquired with a gradient-echo MPRAGE sequence (1.1 mm slice thickness, TR = 2300 ms, TE = 2.8 ms). Diffusion images were acquired using an EPI sequence adapted for tensor measurements and tractography analysis with the following parameters: TE = 104 ms, matrix = 128×128 , FOV = 307×307 mm, voxel size = 2.4 mm isotropic. The scanning included 32 diffusion directions with b -value = 1300 s/mm^2 along with 4 $b = 0 \text{ s/mm}^2$ images. Where available, a peripherally gated sequence was used; otherwise, TR was set to 15 s, approximately matching the effective TR of the gated scans.

HCP-D dataset. The HCP-D dataset is a cross-sectional dataset spanning ages 5–22, collected by the Human Connectome Project in Development (HCP-D)⁷⁸. This dataset was selected for its broad age range, making it highly suitable for studying developmental patterns. Demographic, cognitive, and neuroimaging data from 653 participants were obtained from the NIMH Data Archive (NDA) Lifespan HCP-D release 2.0. After applying several exclusion criteria⁷⁹, 590 participants with complete MRI data and without anatomical abnormalities (273 males; age range, 8.1–21.9) were included in the analysis.

MRI data were collected across four acquisition sites using identical protocols on 3 T SIEMENS Prisma scanners with a 32-channel head coil. The 3D T1-weighted images were acquired at a resolution of 0.8 mm isotropic using a MPRAGE sequence. Two sessions of dMRI scanning were conducted at 1.5 mm isotropic resolution. These sessions employed opposite phase-encoding directions to correct for EPI-induced distortions. Each session included 185 diffusion directions with two b -values (1500 and 3000 s/mm^2) and 14 $b = 0 \text{ s/mm}^2$ images. Additional details on HCP-D acquisition protocol can be found in previous publications⁸⁰.

According to the SAGER (Sex and Gender Equity in Research) guidelines⁸¹, we ensured gender balance in all the three datasets used in this study were balanced in terms of gender, with a well-matched number of male and female participants.

Image preprocessing

HCP dataset. The human T1w structural data had been preprocessed following the HCP's minimal preprocessing pipeline⁷⁷. In brief, the pipeline included imaging alignment to standard volume space using FSL⁸², automatic anatomical surface reconstruction using FreeSurfer⁸³, and registration to a group average surface template space using the multimodal surface matching (MSM) algorithm⁸⁴. Volume data were registered to the Montreal Neurological Institute (MNI) standard space, and surface data were transformed into the surface template space (fs_LR).

Diffusion images were processed using FDT (FMRIB's Diffusion Toolbox) of FSL⁸². The main steps included normalization of the b0 image intensity across runs and correction for EPI susceptibility, eddy-current-induced distortions, gradient-nonlinearities, and subject motion. DTIFIT was then used to fit a diffusion tensor model. The probability distributions of the fiber orientation distribution were estimated using BEDPOSTX⁸⁵.

Next, skull-stripped T1-weighted images for each subject were co-registered to the subject's b0 images using FSL's FLIRT algorithm. Then, nonlinear transformations between the T1w image and the MNI structural template were obtained using FSL's FNIRT. By concatenating these transformations, we derived bi-directional transformations between the diffusion and MNI spaces.

IMAGEN dataset. For the IMAGEN dataset, T1-weighted images were processed using the HCP's minimal preprocessing pipeline. This included alignment to standard volume space using FSL, automatic

anatomical surface reconstruction using FreeSurfer, and registration to a group average surface template space. Volume data were registered to the MNI standard space, and surface data were transformed into the surface template space (fs_LR).

Diffusion MRI was also processed using FDT. The pipeline began with normalizing the b0 intensity, followed by estimating the EPI distortion, eddy current distortions, and subject head motion into a Gaussian process predictor to allow for correction. Then the b0 image was registered to the T1-weighted image using boundary-based registration. Finally, the diffusion data were registered to the native structural space and masked to the appropriate size. In an additional step, FSL's BEDPOSTX⁸⁵ was applied to estimate fiber orientation uncertainty for up to three possible directions per voxel, as done for the HCP dataset. Transformations between diffusion and standard spaces were conducted in the same manner as for the HCP dataset.

HCP-D dataset. Minimally processed T1-weighted images were acquired, which had been processed using the HCP's minimal preprocessing pipeline adapted for children data⁷⁷. Diffusion data preprocessing began with b0 intensity normalization, followed by estimation of EPI distortion, eddy current distortions, and head motion, again modeled using a Gaussian process predictor for correction. The b0 image was registered to the T1w image using boundary-based registration. Diffusion data were then registered to native structural space and masked to the appropriate size. As with the other datasets, BEDPOSTX was applied to estimate fiber orientation uncertainty for up to three possible directions per voxel⁸⁵. Transformations between diffusion and standard spaces were conducted in the same manner as for the HCP dataset.

Construction of tract-geometry coupling

Cortical geometric eigenmodes. We followed the procedure from a previous study to obtain the cortical geometric eigenmodes²¹. The spatial aspect of brain structure satisfies the Laplacian eigenvalue problem, also known as the Helmholtz equation, defined as,

$$\Delta : = \frac{1}{W} \sum_{i,j} \frac{\partial}{\partial x_i} \left(g^{ij} W \frac{\partial}{\partial x_j} \right) \quad (1)$$

where x_i, x_j are the local coordinates, g^{ij} is the inverse of the inner product metric tensor $g_{ij} : = \left(\frac{\partial}{\partial x_i}, \frac{\partial}{\partial x_j} \right)$, $W : = \sqrt{\det(G)}$, \det denoted the determinant, and $G : = (g_{ij})$.

We derived the geometric eigenmodes of the cortical surface by solving the eigen-decomposition problem $\Delta U = U\Lambda$, where U is composed of eigenvectors u_i and the corresponding eigenvalue λ_i . Specifically, we used a triangular surface mesh representation of the gray-white matter interface cortical surface, comprising 32,492 vertices in each hemisphere. For the HCP analysis, we used the published fs_LR 32k surface template (https://github.com/ThomasYeoLab/CBIG/tree/master/data/templates/surface/fs_LR_32k). For the IMAGEN analysis, templates were generated by averaging the reconstructed surfaces of all subjects in FU3.

Connectivity blueprints. To calculate the connectivity blueprints for each subject, we performed probabilistic tractography using FSL's probtrackx2⁸⁶ accelerated via GPUs⁸⁷. Specifically, the white surface was set as the seed region for tracking to the rest of the brain, with the ventricles removed and down-sampled to 3 mm resolution. The pial surface was used as a stop mask to prevent streamlines from crossing sulci. Each vertex was sampled 5000 times (5000 trackings) based on the orientation probability model for each voxel, with a curvature threshold of 0.2, a step length of 0.5 mm, and a number of steps of 3,200. This resulted in a $(\text{whole-surface vertices}) \times (\text{whole-brain voxels})$ matrix.

We utilized probabilistic tractography to quantify the tract-to-cortex patterns, i.e., the tract reachability for each tract segmented by TractSeg²². This approach accounted for the inherent uncertainty in measuring and mapping white matter tracts, providing a more comprehensive and accurate representation of the brain's structural connectivity. Specifically, we reconstructed 72 tracts using a pre-trained deep-learning model, TractSeg²², and down-sampled the resulting tract masks to 3 mm resolution, yielding a $(\text{tracts}) \times (\text{whole-brain voxels})$ matrix. The connectivity blueprints were then generated by multiplying this matrix with the vertex-wise connectivity matrix, followed by normalization²³. The columns of the resulting $(\text{tracts}) \times (\text{whole-surface vertices})$ matrix showed the connectivity distribution pattern of each cortical vertex, while the rows revealed the cortical projection patterns of the tracts, i.e., the tract reachability maps. Note that the superior cerebellar peduncle (SCP), middle cerebellar peduncle (MCP), inferior cerebellar peduncle (ICP), and fornix (FX) were excluded from further analysis due to the absence of cortical projections. Additionally, the overall corpus callosum (CC-all) was excluded because its 7 subsections were already available.

Construction of tract-geometry coupling (TGC). We used the geometric eigenmodes to decompose the reachability maps for the tracts. The orthogonal eigenmodes form a complete basis set, with the corresponding eigenvalues ordered according to the spatial frequency of each mode. For each subject, the reachability map of a tract was reconstructed as a weighted sum of geometric eigenmodes,

$$y = \sum_{i=1}^N a_i u_i \quad (2)$$

where a_i is the amplitude of eigenmode i , u_i is the i^{th} eigenmode, and N is the number of eigenmodes used. The tract-geometry coupling (TGC) was then defined as $TGC := \langle a_1, a_2, \dots, a_N \rangle$. We used $N = 200$ eigenmodes derived from the Helmholtz equation in the current analyses. We used the obtained amplitudes to reconstruct each tract's reachability map and quantified reconstruction accuracy by computing the correlation between empirical and reconstructed data.

Generate surrogate maps for eigenmodes. We used two approaches to randomize the geometric eigenmodes and reconstruct tract reachability maps using surrogate data. We shuffled the eigenmodes to generate 1000 surrogate maps using BrainSMASH²⁶ and eigenstrapping²⁷, both of which preserve intrinsic spatial autocorrelation. We then compared the reconstruction accuracy between the actual and surrogate eigenmodes to test whether the empirical TGC was significantly better than expected by chance.

Characterization of TGC

Individual identification. To explore whether TGC is generally stable across subjects, we calculated the correlation coefficient of TGC between two scans of the same subject in the HCP test-retest dataset, a cohort that underwent two scans over several days ($n = 44$, 12 males; mean age, 30.35 ± 3.76 ; age range, 22–35).

Moreover, we investigated whether TGC could capture individual differences between subjects²⁸. First, a database was created consisting of all individual TGC from the second scan, $D = [X_1^1, X_2^1, \dots, X_2^i, \dots, X_2^N]$, where X_2^i represents the TGC of subject i , and N denotes the number of subjects. To identify the current target matrix X_2^i , similarity was computed between it and all matrices in D , and the predicted identity was the one with the maximum similarity score. Similarity was defined as the Pearson correlation between the target and database matrices. This procedure was also repeated separately for the TGC of each tract.

Definition of high- and low-frequency eigenmodes. Following Preti et al.²⁹, we implemented graph signal filtering to decompose the tract reachability maps into two components: one that was well coupled with geometry (i.e., represented by low-frequency eigenmodes) and one that was less coupled (i.e., high-frequency eigenmodes). The cut-off frequency C was selected by splitting the spectrum into two portions of equal energy (median-split) based on the average energy spectral density. The matrix U^{low} contains the first C eigenmodes (columns of U) complemented with $N-C$ zero columns. In contrast, the matrix U^{high} contains the first C zero columns followed by the remaining $N-C$ eigenmodes. The filtered patterns were obtained using the following equations:

$$\begin{aligned} y^{\text{L}} &= U^{\text{low}} U^{\text{T}} y \\ y^{\text{H}} &= U^{\text{high}} U^{\text{T}} y \end{aligned} \quad (3)$$

Heritability of the TGC. We used APACE to evaluate the heritability of the TGC³⁸, i.e., the proportion of phenotypic variance attributable to genetic factors. We fitted ACE models by partitioning the phenotypic variance into three components: additive genetic effects (A), common or shared environmental factors (C), and unique environmental factors plus measurement error (E). Heritability (h^2) reflects the proportion of phenotypic variance (σ_p^2) accounted for by additive genetic variance (σ_g^2), i.e., $h^2 = \sigma_g^2 / \sigma_p^2$. Phenotypes showing stronger covariances among genetically more similar individuals have higher heritability.

We selected 388 twins from the HCP dataset (102 monozygotic and 92 dizygotic pairs; mean age, 29.96 ± 2.96 ; age range, 22–35) and calculated the heritability of each TGC across subjects. As the TGC is represented as a matrix of dimensions $(\text{tract} \times \text{eigenmode})$, we computed heritability estimates for each element of this matrix, representing the coupling strength between individual white matter tracts and cortical geometric eigenmodes. The heritability of each eigenmode was obtained by averaging heritability values across all tracts. We also assessed heritability between low- and high-frequency eigenmodes in association, commissural, and projection tracts.

Behavioral data of HCP. We tested whether TGC could predict behavior at the individual level. A total of 58 behavioral scores from the HCP were considered. Since many scores were correlated, we performed a principal component analysis, consistent with a previous study³¹, to derive components explaining different behavioral aspects. The top three components explaining the most variance were retained and interpreted as being related to (1) cognition, (2) life dissatisfaction, and (3) emotional recognition.

Behavioral data of IMAGEN. We included four measures of dysfunctional behaviors and six measures of psychopathology symptoms from the IMAGEN dataset (FU3). The four dysfunctional behaviors included two psychiatric symptom scales (Community Assessment of Psychic Experiences [CAPE], Strengths and Difficulties Questionnaires [SDQ]) and 2 addictive behavior measures (the Fagerstrom Test for Nicotine Dependence [FTND], the Alcohol Use Disorders Identification Test [AUDIT]). The primary questions of interest related to lifetime alcohol use and cigarette consumption.

CAPE is a self-report tool used to measure subclinical psychosis phenotypes with good reliability and validity⁸⁹. It captures both positive psychotic experiences and attenuated negative symptoms. Here we used the Total Score CAPE, which is the sum of *Positive Dimension Frequency Score*, *Positive Dimension Distress Score*, *Depressive Dimension Frequency Score*, *Depressive Dimension Distress Score*, *Negative Dimension Frequency Score*, and *Negative Dimension Distress Score*. SDQ is a reliable and valid measure of emotional and behavioral symptoms in youth. It assesses five dimensions of youth pro-social and antisocial behaviors: emotional symptoms, conduct problems, hyperactivity/inattention, peer relationship problems, and

prosocial behavior⁹⁰. Here we used *sebdtot*, which represents the total difficulties score.

For the addictive behavior, we used the FTND and the AUDIT score. The FTND is used to assess nicotine dependence and smoking frequency⁹¹. Here we used *ftnd_sum*, which is the sum of *ftnd1* to *ftnd6*. Higher scores indicate that withdrawal symptoms from quitting tobacco are likely to be stronger. The AUDIT was developed and validated by the World Health Organization to assist with the brief assessment of alcohol use disorders and was specifically designed for international use. Here we used the sum of the *Frequency and Hazardous Alcohol Use*, *Dependence Symptoms* and *Harmful Alcohol Use*.

In addition, six psychopathology symptoms in the IMAGEN dataset were included: depression (*depband*), specific fear (*spphband*), generalised anxiety (*dcgena*), obsessive compulsive disorder (*ocdband*), eating disorder (*eatband*), and exceptionally stressful event (*ptsdband*).

Behavior prediction models. We used kernel ridge regression (KRR) to predict the three behavioral components from the HCP dataset and the IMAGEN behavioral measures, as KRR has demonstrated strong behavioral prediction performance³¹. An L2-regularization term was used to prevent overfitting.

TGC was used as the independent feature in the regression model. We performed 10-fold nested cross-validation for each behavior measure. For each behavior measure, the KRR parameters were estimated from the nine training folds, and the best L2-regularization parameter was selected. This process was repeated across 60 random replications of 10-fold cross-validation to reduce the sensitivity associated with any single partitioning of the data.

Age and gender were regressed out from the behavioral scores within the training folds, and the resulting coefficients were applied to the test fold. Model accuracy was defined as the Pearson correlation coefficient between the predicted and actual behavioral scores in each test fold. Final performance for each behavioral measure was computed by averaging these correlations across folds and replications. A total of 1,000 permutation tests were conducted to assess statistical significance.

Tract reachability was also used as an alternative feature set for behavior prediction, and its performance was compared to that of TGC. Notably, for a fairer comparison between the tract reachability maps and TGC, we used the resulting 200 components for the prediction, which is the same number of eigenmodes used to construct TGC.

Model interpretation. To interpret feature contributions for each behavioral component, we applied the Haufe transformation³². Briefly, for each model, the covariance between each input feature and the predicted behavior score was computed across subjects. A positive feature importance score indicates that higher feature values are associated with higher predicted behavioral scores.

The result was a 7,200-length feature importance vector, which was reshaped into a 200×36 matrix (200 eigenmodes \times 36 tracts). To quantify the contribution of white matter tracts and geometric eigenmodes, we calculated the L2 norm of the TGC contribution across all eigenmodes or all tracts, resulting in an aggregate contribution score for each tract and each eigenmode. This approach enabled us to rank the tracts based on their influence on behavioral prediction, thereby clarifying the roles of different fiber bundles.

High-low frequency ratio of TGC

High-low frequency ratio. As described above, we decomposed the tract reachability maps into two components, y^l and y^h , which were well coupled with geometry (i.e., represented by low-frequency eigenmodes) and were less coupled (i.e., high-frequency eigenmodes), respectively.

As a measure of the tract-geometry coupling for a specific tract, we defined the high-low frequency ratio as the ratio between the norms of y^h and y^l across the vertices where the white matter tract reached the cortical surface. A high-low frequency ratio map was generated for each tract, and an average map was obtained by averaging these maps across tracts.

Functional decoding of the high-low frequency ratio map. We projected meta-analytical task-based activation maps onto the average high-low frequency ratio map to perform functional decoding. Here, we chose 590 terms related to specific cognitive processes that had been selected in previous publications³². The activation maps for the 590 cognitive terms were downloaded from the NeuroSynth database³⁹ (<https://neurosynth.org/>). We generated 20 binarized masks at five-percentile increments of the high-low frequency ratio map. Each of these 20 maps, ranging from 0–5% to 95–100%, was used as inputs to the subsequent meta-analysis. Each function term had a mean activation z-score per bin. The terms included in the visualization were those that had the highest five z-scores in each bin. A significance threshold of $z > 0.5$ was added as a visualization constraint.

Comparison to neurobiological brain maps. To explore the potential biological implications of TGC, we analyzed the relationship between the average high-low frequency ratio map and various brain maps from neuromaps⁴¹. Specifically, we analyzed (i) MEG-derived power maps across canonical frequency bands (theta, alpha, beta, and gamma), reflecting the regional distribution of oscillatory power in resting-state conditions; (ii) the principal functional connectivity (FC) gradient, representing a macroscale axis of cortical organization; and (iii) cortical cerebral blood flow (CBF) map, capturing resting-state perfusion across the cortical mantle.

To examine the neurochemical basis of TGC, we analyzed 19 neurotransmitter receptor maps⁴⁰. These maps include autoradiography and in vivo PET imaging data, covering key neurotransmitter systems such as dopamine (D1, D2), serotonin (5HT1a, 5HT1b, 5HT2a, 5HT4, 5HT6), acetylcholine (M1, M2, VACHT, A4B2), glutamate (mGluR5, NMDA), GABA (GABAA, GABABZ), histamine (H3), cannabinoid (CB1), opioid (MU), and dopamine transporter (DAT). All the maps were obtained in their original coordinate system, so we converted them all to fsaverage_LR32k space.

Spin tests (10,000 times) were used to assess the correspondence between brain maps for the comparisons⁹³. To account for multiple comparisons across the various brain maps tested, we applied the false discovery rate (FDR) correction to the spin-test derived p -values.

Functional associations of TGC

HCP task activation data. We used the task fMRI data from the HCP dataset, projected into 2 mm standard CIFTI grayordinates space. Task data included 86 contrasts from seven task domains⁹⁴: EMOTION, GAMBLING, LANGUAGE, MOTOR, RELATIONAL, SOCIAL, and WORKING MEMORY (WM). Paired negative contrasts were excluded due to redundancy in regression modeling⁹⁵, resulting in 47 contrasts used for further analysis. The z-statistic was used to assess functional activations.

Correlate activation map with TGC. To explore the relationship between task activation and TGC, we first correlated each TGC with each cortical vertex across subjects. Significant associations were defined as those with $p < 0.05$, corrected for multiple comparisons using FDR. The number of significant vertices was then used to represent the strength of association between each TGC and the activation map. We also computed the correlation between the above-mentioned uncorrected correlation matrix and the activation map.

TGC with higher correlation values were interpreted as having a stronger association with the activation map.

Developmental trajectory of TGC

Two developmental datasets were used in the investigation of development of TGC, i.e., the HCP-D dataset ($n = 590$; age range, 8–22 y) and the IMAGEN dataset ($n = 661$; age range, 14–23 y). Tract reachability maps were derived as previously described. For each subject and tract, the L1-norm value of the TGC was calculated to quantify the total coupling strength with cortical geometry.

We used generalized additive models (GAMs) to assess the developmental trajectories of TGC L1-norm values from age 8 to 22, allowing for both linear and nonlinear effects of age. Statistical analyses were conducted in R 4.1.0, with GAMs being fitted using the mgcv package⁹⁶. The GAM model included TGC L1-norm as the dependent variable, age as a smooth term, and gender and site as covariates,

$$TGC \sim s(\text{Age}) + \text{Sex} + \text{Site} \quad (4)$$

To visualize developmental trajectories of tracts, we predicted the model fits at 1000 age points evenly sampled across the age span. The GAM-fitting process generated smooth developmental curves, illustrating developmental changes in TGC for each tract. Age effects (ΔR^2) were assessed by comparing the R^2 values of the full model, which included the age smooth term, with a reduced model that excluded the age smooth term. Bonferroni correction was applied to all GAM models to adjust for multiple comparisons.

The first derivative of each GAM age spline was computed, and the average derivative over adolescence (8–22 years) was used as the increase rate of each tract. Increase rates were compared across tract types using the Mann-Whitney U test. To verify findings, the same analysis was replicated using the IMAGEN dataset.

Reporting summary

Further information on research design is available in the Nature Portfolio Reporting Summary linked to this article.

Data availability

HCP data are available at <https://db.humanconnectome.org/>. IMAGEN data are available at <https://imagen2.cea.fr/>. HCP-D data are available at <https://www.humanconnectome.org/study/hcp-lifespan-development/data-releases>. The activated maps of the cognitive terms can be downloaded from the NeuroSynth database (<https://neurosynth.org/>). Source data are provided with this paper.

Code availability

The HCP-Pipeline can be found at <https://github.com/Washington-University/HCPpipelines>. The neuroimaging preprocessing software used for the other datasets is freely available (FreeSurfer v7.3.2, <http://surfer.nmr.mgh.harvard.edu/> and FSL v6.0.7, <https://fsl.fmrib.ox.ac.uk/fsl/fslwiki>). The brain maps were presented using BrainSpace (<https://brainspace.readthedocs.io/>) and Connectome Workbench v1.5.0 (<https://www.humanconnectome.org/software/connectome-workbench/>). The tracts were presented using BrainNet Viewer v1.7 (<https://www.nitrc.org/projects/bnv/>). Generalized additive models (GAM) were fit using mgcv package in R (version 4.1.0). The code to generate the results in this work is available at https://github.com/FANLabCASA/D_TGC_tract-geometry-coupling.git.

References

- Bullock, D. N. et al. A taxonomy of the brain's white matter: twenty-one major tracts for the 21st century. *Cereb. Cortex* **32**, 4524–4548 (2022).
- Yeh, F. C. Population-based tract-to-region connectome of the human brain and its hierarchical topology. *Nat. Commun.* **13**, 4933 (2022).
- Honey, C. J. et al. Predicting human resting-state functional connectivity from structural connectivity. *Proc. Natl. Acad. Sci. USA* **106**, 2035–2040 (2009).
- Suarez, L. E., Markello, R. D., Betzel, R. F. & Misic, B. Linking structure and function in macroscale brain networks. *Trends Cogn. Sci.* **24**, 302–315 (2020).
- Eichert, N. et al. Cross-species cortical alignment identifies different types of anatomical reorganization in the primate temporal lobe. *Elife* **9**, <https://doi.org/10.7554/eLife.53232> (2020).
- Warrington, S. et al. Concurrent mapping of brain ontogeny and phylogeny within a common space: Standardized tractography and applications. *Sci. Adv.* **8**, eabq2022 (2022).
- Yeh, F. C. et al. Population-averaged atlas of the macroscale human structural connectome and its network topology. *Neuroimage* **178**, 57–68 (2018).
- Zhang, Z. et al. Mapping population-based structural connectomes. *Neuroimage* **172**, 130–145 (2018).
- Van Essen, D. C. A tension-based theory of morphogenesis and compact wiring in the central nervous system. *Nature* **385**, 313–318 (1997).
- Van Essen, D. C. A 2020 view of tension-based cortical morphogenesis. *Proc. Natl. Acad. Sci. USA* **117**, 32868–32879 (2020).
- Fernandez, V., Llinares-Benadero, C. & Borrell, V. Cerebral cortex expansion and folding: what have we learned?. *EMBO J.* **35**, 1021–1044 (2016).
- Garcia, K. E., Kroenke, C. D. & Bayly, P. V. Mechanics of cortical folding: stress, growth and stability. *Philos. Trans. R Soc. Lond. B Biol. Sci.* **373**, <https://doi.org/10.1098/rstb.2017.0321> (2018).
- Takahashi, E., Folkerth, R. D., Galaburda, A. M. & Grant, P. E. Emerging cerebral connectivity in the human fetal brain: an MR tractography study. *Cereb. Cortex* **22**, 455–464 (2012).
- Garcia, K. E., Wang, X. & Kroenke, C. D. A model of tension-induced fiber growth predicts white matter organization during brain folding. *Nat. Commun.* **12**, 6681 (2021).
- Kostovic, I. & Rakic, P. Developmental history of the transient subplate zone in the visual and somatosensory cortex of the macaque monkey and human brain. *J. Comp. Neurol.* **297**, 441–470 (1990).
- Zhang, S. et al. Species-shared and -unique gyral peaks on human and macaque brains. *Elife* **12**, <https://doi.org/10.7554/eLife.90182> (2024).
- Schwartz, E. et al. Evolution of cortical geometry and its link to function, behaviour and ecology. *Nat. Commun.* **14**, 2252 (2023).
- Dall'Acqua, P. et al. Connectomic and surface-based morphometric correlates of acute mild traumatic brain injury. *Front Hum. Neurosci.* **10**, 127 (2016).
- Rakic, P. Specification of cerebral cortical areas. *Science* **241**, 170–176 (1988).
- Chen, Y. C. et al. The individuality of shape asymmetries of the human cerebral cortex. *Elife* **11**, <https://doi.org/10.7554/eLife.75056> (2022).
- Pang, J. C. et al. Geometric constraints on human brain function. *Nature* **618**, 566–574 (2023).
- Wasserthal, J., Neher, P. & Maier-Hein, K. H. TractSeg - Fast and accurate white matter tract segmentation. *Neuroimage* **183**, 239–253 (2018).
- Mars, R. B. et al. Whole brain comparative anatomy using connectivity blueprints. *Elife* **7**, <https://doi.org/10.7554/eLife.35237> (2018).
- Van Essen, D. C. et al. The WU-Minn Human Connectome Project: an overview. *Neuroimage* **80**, 62–79 (2013).

25. Schumann, G. et al. The IMAGEN study: reinforcement-related behaviour in normal brain function and psychopathology. *Mol. Psychiatry* **15**, 1128–1139 (2010).
26. Burt, J. B., Helmer, M., Shinn, M., Anticevic, A. & Murray, J. D. Generative modeling of brain maps with spatial autocorrelation. *Neuroimage* **220**, 117038 (2020).
27. Koussis, N. C. et al. Generation of surrogate brain maps preserving spatial autocorrelation through random rotation of geometric eigenmodes. *Imaging Neuroscience* **3**, IMAG.a.71 (2025).
28. Finn, E. S. et al. Functional connectome fingerprinting: identifying individuals using patterns of brain connectivity. *Nat. Neurosci.* **18**, 1664–1671 (2015).
29. Preti, M. G. & Van De Ville, D. Decoupling of brain function from structure reveals regional behavioral specialization in humans. *Nat. Commun.* **10**, 4747 (2019).
30. Kong, R. et al. Spatial topography of individual-specific cortical networks predicts human cognition, personality, and emotion. *Cereb. Cortex* **29**, 2533–2551 (2019).
31. Ooi, L. Q. R. et al. Comparison of individualized behavioral predictions across anatomical, diffusion and functional connectivity MRI. *Neuroimage* **263**, 119636 (2022).
32. Haufe, S. et al. On the interpretation of weight vectors of linear models in multivariate neuroimaging. *Neuroimage* **87**, 96–110 (2014).
33. Miller, E. K. & Cohen, J. D. An integrative theory of prefrontal cortex function. *Annu. Rev. Neurosci.* **24**, 167–202 (2001).
34. Dhamala, E., Jamison, K. W., Jaywant, A., Dennis, S. & Kuceyeski, A. Distinct functional and structural connections predict crystallised and fluid cognition in healthy adults. *Hum. Brain Mapp.* **42**, 3102–3118 (2021).
35. Glasser, M. F. et al. A multi-modal parcellation of human cerebral cortex. *Nature* **536**, 171–178 (2016).
36. Assem, M., Glasser, M. F., Van Essen, D. C. & Duncan, J. A domain-general cognitive core defined in multimodally parcellated human cortex. *Cereb. Cortex* **30**, 4361–4380 (2020).
37. Ji, J. L. et al. Mapping the human brain's cortical-subcortical functional network organization. *Neuroimage* **185**, 35–57 (2019).
38. Fan, L. et al. The Human Brainnetome Atlas: a new brain atlas based on connectional architecture. *Cereb. Cortex* **26**, 3508–3526 (2016).
39. Yarkoni, T., Poldrack, R. A., Nichols, T. E., Van Essen, D. C. & Wager, T. D. Large-scale automated synthesis of human functional neuroimaging data. *Nat. Methods* **8**, 665–670 (2011).
40. Hansen, J. Y. et al. Mapping neurotransmitter systems to the structural and functional organization of the human neocortex. *Nat. Neurosci.* **25**, 1569–1581 (2022).
41. Markello, R. D. et al. neuromaps: structural and functional interpretation of brain maps. *Nat. Methods* **19**, 1472–1479 (2022).
42. Chavoshnejad, P. et al. Role of axonal fibers in the cortical folding patterns: a tale of variability and regularity. *Brain Multiphys.* **2**, 100029 (2021).
43. Liang, X. et al. Structural connectome architecture shapes the maturation of cortical morphology from childhood to adolescence. *Nat. Commun.* **15**, 784 (2024).
44. Cafiero, R., Brauer, J., Anwender, A. & Friederici, A. D. The concurrence of cortical surface area expansion and white matter myelination in human brain development. *Cereb. Cortex* **29**, 827–837 (2019).
45. Walhovd, K. B., Fjell, A. M., Giedd, J., Dale, A. M. & Brown, T. T. Through thick and thin: a need to reconcile contradictory results on trajectories in human cortical development. *Cereb. Cortex* **27**, 1472–1481 (2017).
46. Natu, V. S. et al. Apparent thinning of human visual cortex during childhood is associated with myelination. *Proc. Natl. Acad. Sci. USA* **116**, 20750–20759 (2019).
47. Bryant, K. L., Li, L., Eichert, N. & Mars, R. B. A comprehensive atlas of white matter tracts in the chimpanzee. *PLoS Biol.* **18**, e3000971 (2020).
48. Jeon, T., Mishra, V., Ouyang, M., Chen, M. & Huang, H. Synchronous changes of cortical thickness and corresponding white matter microstructure during brain development accessed by diffusion MRI tractography from parcellated cortex. *Front. Neuroanat.* **9**, 158 (2015).
49. Beul, S. F., Grant, S. & Hilgetag, C. C. A predictive model of the cat cortical connectome based on cytoarchitecture and distance. *Brain Struct. Funct.* **220**, 3167–3184 (2015).
50. Moore, J. K. & Guan, Y. L. Cytoarchitectural and axonal maturation in human auditory cortex. *J. Assoc. Res. Otolaryngol.* **2**, 297–311 (2001).
51. Gomez, J. et al. Microstructural proliferation in human cortex is coupled with the development of face processing. *Science* **355**, 68–71 (2017).
52. Mayer, S. et al. Multimodal single-cell analysis reveals physiological maturation in the developing human neocortex. *Neuron* **102**, 143–158 e147 (2019).
53. Becker, Y., Loh, K. K., Coulon, O. & Meguerditchian, A. The Arcuate Fasciculus and language origins: Disentangling existing conceptions that influence evolutionary accounts. *Neurosci. Biobehav. Rev.* **134**, 104490 (2022).
54. Von Der Heide, R. J., Skipper, L. M., Klobusicky, E. & Olson, I. R. Dissecting the uncinate fasciculus: disorders, controversies and a hypothesis. *Brain* **136**, 1692–1707 (2013).
55. Menjot de Champfleury, N. et al. Middle longitudinal fasciculus delineation within language pathways: a diffusion tensor imaging study in human. *Eur. J. Radio.* **82**, 151–157 (2013).
56. Jung, S. et al. Uncinate fasciculus white matter connectivity related to impaired social perception and cross-sectional and longitudinal symptoms in patients with schizophrenia spectrum psychosis. *Neurosci. Lett.* **737**, 135144 (2020).
57. Chawla, N., Deep, R., Khandelwal, S. K. & Garg, A. Reduced integrity of superior longitudinal fasciculus and arcuate fasciculus as a marker for auditory hallucinations in schizophrenia: a DTI tractography study. *Asian J. Psychiatr.* **44**, 179–186 (2019).
58. Xu, E. P., Nguyen, L., Leibenluft, E., Stange, J. P. & Linke, J. O. A meta-analysis on the uncinate fasciculus in depression. *Psychol. Med.* **53**, 2721–2731 (2023).
59. Li, D. et al. Topographic axes of wiring space converge to genetic topography in shaping the human cortical layout. *J. Neurosci.* **45**, <https://doi.org/10.1523/JNEUROSCI.1510-24.2024> (2025).
60. Ashwell, K. W., Waite, P. M. & Marotte, L. Ontogeny of the projection tracts and commissural fibres in the forebrain of the tammar wallaby (*Macropus eugenii*): timing in comparison with other mammals. *Brain Behav. Evol.* **47**, 8–22 (1996).
61. Lebel, C. et al. Diffusion tensor imaging of white matter tract evolution over the lifespan. *Neuroimage* **60**, 340–352 (2012).
62. Graziano, P. A., Garic, D. & Dick, A. S. Individual differences in white matter of the uncinate fasciculus and inferior fronto-occipital fasciculus: possible early biomarkers for callous-unemotional behaviors in young children with disruptive behavior problems. *J. Child Psychol. Psychiatry* **63**, 19–33 (2022).
63. Teipel, S. J. et al. White matter microstructure underlying default mode network connectivity in the human brain. *Neuroimage* **49**, 2021–2032 (2010).
64. Wu, D. et al. Hierarchy of connectivity-function relationship of the human cortex revealed through predicting activity across functional domains. *Cereb. Cortex* **30**, 4607–4616 (2020).
65. Fields, R. D. White matter in learning, cognition and psychiatric disorders. *Trends Neurosci.* **31**, 361–370 (2008).
66. Deco, G. et al. How local excitation-inhibition ratio impacts the whole brain dynamics. *J. Neurosci.* **34**, 7886–7898 (2014).

67. Deco, G. et al. Resting-state functional connectivity emerges from structurally and dynamically shaped slow linear fluctuations. *J. Neurosci.* **33**, 11239–11252 (2013).
68. Gu, S. et al. Controllability of structural brain networks. *Nat. Commun.* **6**, 8414 (2015).
69. Tang, E. et al. Developmental increases in white matter network controllability support a growing diversity of brain dynamics. *Nat. Commun.* **8**, 1252 (2017).
70. Maier-Hein, K. H. et al. The challenge of mapping the human connectome based on diffusion tractography. *Nat. Commun.* **8**, 1349 (2017).
71. Thomas, C. et al. Anatomical accuracy of brain connections derived from diffusion MRI tractography is inherently limited. *Proc. Natl. Acad. Sci. USA* **111**, 16574–16579 (2014).
72. Reveley, C. et al. Superficial white matter fiber systems impede detection of long-range cortical connections in diffusion MR tractography. *Proc. Natl. Acad. Sci. USA* **112**, E2820–E2828 (2015).
73. Zhang, F. et al. Quantitative mapping of the brain's structural connectivity using diffusion MRI tractography: a review. *Neuroimage* **249**, 118870 (2022).
74. Jbabdi, S., Sotiropoulos, S. N., Haber, S. N., Van Essen, D. C. & Behrens, T. E. Measuring macroscopic brain connections in vivo. *Nat. Neurosci.* **18**, 1546–1555 (2015).
75. Bu, X., Cao, M., Huang, X. & He, Y. The structural connectome in ADHD. *Psychoradiology* **1**, 257–271 (2021).
76. Ecker, C., Bookheimer, S. Y. & Murphy, D. G. Neuroimaging in autism spectrum disorder: brain structure and function across the lifespan. *Lancet Neurol.* **14**, 1121–1134 (2015).
77. Glasser, M. F. et al. The minimal preprocessing pipelines for the Human Connectome Project. *Neuroimage* **80**, 105–124 (2013).
78. Somerville, L. H. et al. The Lifespan Human Connectome Project in Development: A large-scale study of brain connectivity development in 5–21 year olds. *Neuroimage* **183**, 456–468 (2018).
79. Xu, X., Yang, H., Cong, J., Sydnor, V. & Cui, Z. Structural connectivity matures along a sensorimotor-association connective axis in youth. *bioRxiv*, <https://doi.org/10.1101/2024.06.17.599267> (2024).
80. Harms, M. P. et al. Extending the Human Connectome Project across ages: Imaging protocols for the Lifespan Development and Aging projects. *Neuroimage* **183**, 972–984 (2018).
81. Heidari, S., Babor, T. F., De Castro, P., Tort, S. & Curno, M. Sex and Gender Equity in Research: rationale for the SAGER guidelines and recommended use. *Res. Integr. Peer Rev.* **1**, 2 (2016).
82. Jenkinson, M., Beckmann, C. F., Behrens, T. E., Woolrich, M. W. & Smith, S. M. *Fsl. Neuroimage* **62**, 782–790 (2012).
83. Fischl, B. FreeSurfer. *Neuroimage* **62**, 774–781 (2012).
84. Robinson, E. C. et al. Multimodal surface matching with higher-order smoothness constraints. *Neuroimage* **167**, 453–465 (2018).
85. Behrens, T. E. et al. Characterization and propagation of uncertainty in diffusion-weighted MR imaging. *Magn. Reson. Med.* **50**, 1077–1088 (2003).
86. Behrens, T. E., Berg, H. J., Jbabdi, S., Rushworth, M. F. & Woolrich, M. W. Probabilistic diffusion tractography with multiple fibre orientations: What can we gain?. *Neuroimage* **34**, 144–155 (2007).
87. Hernandez-Fernandez, M. et al. Using GPUs to accelerate computational diffusion MRI: from microstructure estimation to tractography and connectomes. *Neuroimage* **188**, 598–615 (2019).
88. Chen, X. et al. Accelerated estimation and permutation inference for ACE modeling. *Hum. Brain Mapp.* **40**, 3488–3507 (2019).
89. van Os, J. et al. Cannabis use and psychosis: a longitudinal population-based study. *Am. J. Epidemiol.* **156**, 319–327 (2002).
90. Goodman, R. The strengths and difficulties questionnaire: a research note. *J. Child Psychol. Psychiatry* **38**, 581–586 (1997).
91. Heatherton, T. F., Kozlowski, L. T., Frecker, R. C. & Fagerstrom, K. O. The Fagerstrom test for nicotine dependence: a revision of the fagerstrom tolerance questionnaire. *Br. J. Addict.* **86**, 1119–1127 (1991).
92. Karolis, V. R., Corbetta, M. & Thiebaut de Schotten, M. The architecture of functional lateralisation and its relationship to callosal connectivity in the human brain. *Nat. Commun.* **10**, 1417 (2019).
93. Alexander-Bloch, A. F. et al. On testing for spatial correspondence between maps of human brain structure and function. *Neuroimage* **178**, 540–551 (2018).
94. Barch, D. M. et al. Function in the human connectome: task-fMRI and individual differences in behavior. *Neuroimage* **80**, 169–189 (2013).
95. Tavor, I. et al. Task-free MRI predicts individual differences in brain activity during task performance. *Science* **352**, 216–220 (2016).
96. Wood, S. N. Stable and efficient multiple smoothing parameter estimation for generalized additive models. *J. Am. Stat. Assoc.* **99**, 673–686 (2004).

Acknowledgements

This work was partially supported by STI2030-Major Projects (Grant No. 2021ZD0200200 to L.F.), the Natural Science Foundation of China (Grant Nos. 82472061 to L.F., 82202253 to L.C., 62250058 to C.C.), and Chongqing Science and Health Joint Medical Research Key Project (2025GGXM005 to L.F.), and Guangxi Natural Science Foundation (Grant No. 2024GXNSFBA010212 to L.C.). Data were provided in part by the Human Connectome Project, WU-Minn Consortium (Principal Investigators: David Van Essen and Kamil Ugurbil; 1U54MH091657), which was funded by the 16 NIH Institutes and Centers that support the NIH Blueprint for Neuroscience Research and by the McDonnell Center for Systems Neuroscience at Washington University; the European Union-funded FP6 Integrated Project IMAGEN (Reinforcement-related behaviour in normal brain function and psychopathology) (LSHM-CT-2007-037286), the Horizon 2020 funded ERC Advanced Grant 'STRATIFY' (Brain network based stratification of reinforcement-related disorders) (695313), Horizon Europe 'enviROMENTAL', grant no: 101057429, UK Research and Innovation (UKRI) Horizon Europe funding guarantee (10041392 and 10038599), Human Brain Project (HBP SGA 2, 785907, and HBP SGA 3, 945539), the Chinese government via the Ministry of Science and Technology (MOST). The German Center for Mental Health (DZPG), the Bundesministerium für Bildung und Forschung (BMBF grants 01GS08152; 01EV0711; Forschungsnetz AERIAL 01EE1406A, 01EE1406B; Forschungsnetz IMAC-Mind 01GL1745B), the Deutsche Forschungsgemeinschaft (DFG grants SM 80/7-2, SFB 940, TRR 265, NE 1383/14-1, 186318919 [FOR 1617], 178833530 [SFB 940], 386691645 [NE 1383/14-1], 402170461 [TRR 265], 454245598 [IRTG 2773]), the Medical Research Foundation and Medical Research Council (grants MR/R00465X/1 and MR/S020306/1), the National Institutes of Health (NIH) funded ENIGMA-grants 5U54EB020403-05, 1R56AG058854-01 and U54 EB020403 as well as NIH R01DA049238, the National Institutes of Health, Science Foundation Ireland (16/ERC/D/3797). NSFC grant 82150710554. Further support was provided by grants from: - the ANR (ANR-12-SAMA-0004, AAPG2019 - GeBra), the Eranet Neon (AF12-NEURO0008-01 - WM2NA; and ANR-18-NEURO0002-01 - ADORé), the Fondation de France (00081242), the Fondation pour la Recherche Médicale (DPA20140629802), the Mission Interministérielle de Lutte-contre-les-Drogues-et-les-Conduites-Addictives (MILDECA), the Assistance-Publique-Hôpitaux-de-Paris and INSERM (interface grant), Paris Sud University IDEX 2012, the Fondation de l'Avenir (grant AP-RM-17-013), the Fédération pour la Recherche sur le Cerveau, the Ile de France region (grant QIM VEAVE convention 23002745-23002747). The authors appreciate the English language and editing assistance of Rhoda E. and Edmund F. Perozzi, PhDs. The authors appreciate the illustration refinement and contribution to the icon design of Lit-ing Zheng.

Author contributions

D.L. performed the experimental studies; D.L. wrote the paper; A.Z., Y.W., C.C., and L.F. revised the paper; H.W. contributed by preprocessing the neuroimaging data; A.Z., Y.W., T.J., C.C., and L.F. provided theoretical guidance and informed interpretation of the results; L.M. and L.C. contributed analytic tools; T.B., G.B., A.B., R.B., S.D., H.F., H.G., P.G., A.G., A.H., H.L., J.M., M.M., E.A., F.N., D.O., L.P., M.S., N.V., H.W., R.W., G.S., and T.J. contributed to the collection of the IMAGEN cohorts as members of the IMAGEN Consortium; C.C. and L.F. supervised the overall work.

Competing interests

Dr Banaschewski served in an advisory or consultancy role for Lundbeck, Medice, Neurim Pharmaceuticals, Oberberg GmbH, Shire. He received conference support or speaker's fee by Lilly, Medice, Novartis, and Shire. He has been involved in clinical trials conducted by Shire & Viforpharma. He received royalties from Hogrefe, Kohlhammer, CIP Medien, Oxford University Press. The present work is unrelated to the above grants and relationships. Dr Barker has received honoraria from General Electric Healthcare for teaching on scanner programming courses. Dr Poustka served in an advisory or consultancy role for Roche and Viforpharm and received speaker's fee by Shire. She received royalties from Hogrefe, Kohlhammer, and Schattauer. The present work is unrelated to the above grants and relationships. The other authors report no biomedical financial interests or potential conflicts of interest.

Additional information

Supplementary information The online version contains supplementary material available at <https://doi.org/10.1038/s41467-025-62812-9>.

Correspondence and requests for materials should be addressed to Congying Chu or Lingzhong Fan.

Peer review information *Nature Communications* thanks the anonymous reviewer(s) for their contribution to the peer review of this work. A peer review file is available.

Reprints and permissions information is available at <http://www.nature.com/reprints>



Publisher's note Springer Nature remains neutral with regard to jurisdictional claims in published maps and institutional affiliations.

Open Access This article is licensed under a Creative Commons Attribution-NonCommercial-NoDerivatives 4.0 International License, which permits any non-commercial use, sharing, distribution and reproduction in any medium or format, as long as you give appropriate credit to the original author(s) and the source, provide a link to the Creative Commons licence, and indicate if you modified the licensed material. You do not have permission under this licence to share adapted material derived from this article or parts of it. The images or other third party material in this article are included in the article's Creative Commons licence, unless indicated otherwise in a credit line to the material. If material is not included in the article's Creative Commons licence and your intended use is not permitted by statutory regulation or exceeds the permitted use, you will need to obtain permission directly from the copyright holder. To view a copy of this licence, visit <http://creativecommons.org/licenses/by-nc-nd/4.0/>.

© The Author(s) 2025

¹Beijing Key Laboratory of Brainnetome and Brain-Computer Interface, Institute of Automation, Chinese Academy of Sciences, Beijing, China. ²Brainnetome Center, Institute of Automation, Chinese Academy of Sciences, Beijing, China. ³School of Artificial Intelligence, University of Chinese Academy of Sciences, Beijing, China. ⁴Systems Lab, Department of Psychiatry, The University of Melbourne, Victoria, VIC, Australia. ⁵Department of Biomedical Engineering, The University of Melbourne, Victoria, VIC, Australia. ⁶School of Life and Environmental Sciences, Guilin University of Electronic Technology, Guilin, China. ⁷Department of Child and Adolescent Psychiatry and Psychotherapy, Central Institute of Mental Health, Medical Faculty Mannheim, Heidelberg University, German Center for Mental Health (DZPG), Mannheim, Germany. ⁸Department of Neuroimaging, Institute of Psychiatry, Psychology & Neuroscience, King's College London, London, UK. ⁹Discipline of Psychiatry, School of Medicine and Trinity College Institute of Neuroscience, Trinity College Dublin, Dublin, Ireland. ¹⁰Physikalisch-Technische Bundesanstalt (PTB), Braunschweig and Berlin, Berlin, Germany. ¹¹Social, Genetic and Developmental Psychiatry Centre, Institute of Psychiatry, Psychology & Neuroscience, King's College London, London, UK. ¹²Institute of Cognitive and Clinical Neuroscience, Central Institute of Mental Health, Medical Faculty Mannheim, Heidelberg University, Mannheim, Germany. ¹³Department of Psychology, School of Social Sciences, University of Mannheim, Mannheim, Germany. ¹⁴Departments of Psychiatry and Psychology, University of Vermont, Burlington, VT, USA. ¹⁵Sir Peter Mansfield Imaging Centre School of Physics and Astronomy, University of Nottingham, University Park, Nottingham, UK. ¹⁶NeuroSpin, CEA, Université Paris-Saclay, Gif-sur-Yvette, France. ¹⁷Department of Psychiatry and Psychotherapy CCM, Charité—Universitätsmedizin Berlin, corporate member of Freie Universität Berlin, Humboldt-Universität zu Berlin and Berlin Institute of Health, Berlin, Germany. ¹⁸Institut des Maladies Neurodégénératives, UMR 5293, CNRS, CEA, Université de Bordeaux, Bordeaux, France. ¹⁹Institut National de la Santé et de la Recherche Médicale, INSERM U1299 "Trajectoires développementales & psychiatrie", University Paris-Saclay, Ecole Normale Supérieure Paris-Saclay; Centre Borelli CNRS 9010, Gif-sur-Yvette, France. ²⁰AP-HP, Sorbonne Université, Department of Child and Adolescent Psychiatry, Pitié-Salpêtrière Hospital, Paris, France. ²¹Psychiatry Department, EPS Barthélémy Durand, Etampes, France. ²²Institute of Medical Psychology and Medical Sociology, University Medical Center Schleswig Holstein, Kiel University, Kiel, Germany. ²³Department of Child and Adolescent Psychiatry, Center for Psychosocial Medicine, University Hospital Heidelberg, Heidelberg, Germany. ²⁴Department of Psychiatry and Psychotherapy, Technische Universität Dresden, Dresden, Germany. ²⁵Centre for Population Neuroscience and Stratified Medicine (PONS), Department of Psychiatry and Psychotherapy, Charité Universitätsmedizin Berlin, Burlington, Germany. ²⁶School of Psychology and Global Brain Health Institute, Trinity College Dublin, Dublin, Ireland. ²⁷Centre for Population Neuroscience and Precision Medicine (PONS), Institute for Science and Technology of Brain-Inspired Intelligence (ISTBI), Fudan University, Shanghai, China. ²⁸Institute of Science and Technology for Brain-Inspired Intelligence (Fudan University), Shanghai, China. ²⁹Ministry of Education, Key Laboratory of Computational Neuroscience and Brain-Inspired Intelligence (Fudan University), Shanghai, China. ³⁰Centre for Population Neuroscience and Precision Medicine (PONS), Institute of Psychiatry, Psychology & Neuroscience, SGDP Centre, King's College London, London, UK. ³¹School of Life Sciences and Health, University of Health and Rehabilitation Sciences, Qingdao, China. ³²Shandong Key Lab of Complex Medical Intelligence and Aging, Binzhou Medical University, Yantai, China. ✉ e-mail: congying.chu@ia.ac.cn; lingzhong.fan@ia.ac.cn

IMAGEN Consortium

Tobias Banaschewski ⁷, Gareth J. Barker ⁸, Arun L. W. Bokde ⁹, Rüdiger Brühl ¹⁰, Sylvane Desrivières ¹¹, Herta Flor ^{12,13}, Hugh Garavan ¹⁴, Penny Gowland ¹⁵, Antoine Grigis¹⁶, Andreas Heinz ¹⁷, Hervé Lemaître ^{16,18}, Jean-Luc Martinot ¹⁹, Marie-Laure Paillère Martinot^{19,20}, Eric Artiges ^{19,21}, Frauke Nees ^{7,22}, Dimitri Papadopoulos Orfanos ¹³, Luise Poustka²³, Michael N. Smolka ²⁴, Nilakshi Vaidya ²⁵, Henrik Walter ¹⁷, Robert Whelan ²⁶, Gunter Schumann ^{24,27} & Tianye Jia ^{27,28,29,30}